Separating atmospheric and ocean-mediated impacts of time-evolving industrial and biomass burning aerosols on historical boreal summer climate

Xueying Zhao[a,b*], Clara Deser[a], Geeta Persad[b], Adam S. Phillips[a], Kayla White[b], and Nan Rosenbloom[a]

[a] *NSF National Center for Atmospheric Research, Boulder CO*

[b] *Jackson School of Geosciences, The University of Texas at Austin, Austin TX*

* *Corresponding author*: Dr. Xueying Zhao, Climate and Global Dynamics Laboratory, NCAR, 1850 Table Mesa Drive, Boulder CO 80305, xueying.zhao@jsg.utexas.edu

Submitted to *Journal of Climate*

Revised April 2, 2026

ABSTRACT

The spatial pattern of industrial aerosol emissions has changed markedly over the past century, alongside regional shifts in biomass burning (BMB) sources. While previous studies examined evolving industrial aerosol effects, the relative contributions of atmospheric radiative *vs.* ocean-mediated responses to combined aerosol sources remain unclear. Using global atmosphere-land simulations driven by time-evolving historical industrial and BMB aerosol emissions and aerosol-induced sea surface temperature (SST) anomalies, we identify two leading modes of multi-decadal aerosol optical depth (AOD) variability in boreal summer, together accounting for 94% of the AOD variance from 1930-2030. Mode 1 depicts a monotonic increase over low latitudes, while Mode 2 describes a sinusoidal trajectory over Northern Hemisphere continents with weaker opposite changes over South and East Asia. These AOD modes drive distinct atmospheric circulation, precipitation and land surface air temperature responses. We separate the atmospheric radiative and ocean-mediated pathways of response through a novel experimental design based on Community Atmosphere Model version 5 forced with time-evolving aerosol emissions and aerosol-induced SSTs individually and in combination; aerosol-induced SSTs are derived from the Community Earth System Model version 1 Single-Forcing and All-Forcing Large Ensembles. We find that ocean-mediated effects dominate the large-scale atmospheric circulation and precipitation responses, while atmospheric radiative effects induce robust regional impacts and modulate the ocean-mediated response in remote regions. Our results demonstrate that transient aerosol impacts reflect a dynamic balance between atmospheric radiative and ocean-mediated pathways of response, and highlight the importance of considering the evolving spatial pattern of aerosol forcing when assessing aerosol-driven climate variations.

SIGNIFICANCE STATEMENT

Aerosols from industrial activities and biomass burning have changed significantly over the 20th century. We conduct a novel set of climate model simulations to investigate how the changing spatial distribution of these aerosol emissions influenced historical climate via atmospheric and oceanic pathways. Using a pattern-based approach, we find that these aerosols influence global climate by modifying ocean surface temperatures, which in turn drive changes in global-scale atmospheric circulation, affecting precipitation and land surface air temperature. Aerosols' interaction with radiation in the atmosphere drives local and regional

impacts and modulates oceanic-driven responses in remote regions. Our results highlight the importance of evolving aerosol patterns in shaping historical anthropogenic climate change and underscore the complexity of atmospheric and oceanic pathways governing the responses.

1. Introduction

Aerosols from anthropogenic sources are one of the dominant drivers of climate change over the industrial era (IPCC AR6, 2021). Aerosols from industrial sources have played a key role in shaping historical patterns of forced climate change in the atmosphere and ocean, with impacts on regional temperature and precipitation (e.g., Dong et al. 2024; Shi et al. 2022; Kang et al. 2021; Deser et al. 2020; Xie et al. 2013). For instance, Northern Hemisphere (NH) industrial aerosol emissions have been linked to the observed southward shift of the tropical Pacific and Atlantic rain belts in the late 20th century (Ming and Ramaswamy, 2011; Hwang et al., 2013; Hill et al., 2015; Allen et al., 2015). Aerosols from industrial sources, including those at lower latitudes, have also contributed to the weakening of South and East Asian Summer Monsoon circulations and the associated decrease in monsoon precipitation (Bollasina et al., 2011, 2014), as well as Sahel drought and subsequent recovery (Hua et al. 2019; Hirasawa et al., 2020). Industrial aerosol emissions have also been implicated in the recent weakening of the NH summertime atmospheric circulation, including the upper-level jet stream (Dong et al., 2022) and storm tracks (Kang et al., 2024; Chemke and Coumou, 2024). In addition, the historical NH mid-latitude aerosol increase has been suggested to delay the emergence of Arctic amplification until the past few decades (Mueller et al., 2018; England et al., 2021) while their reductions after the 1980s are linked to recent enhanced summer warming in western Europe (Schumacher et al., 2024; Roesch et al., 2025). Furthermore, industrial aerosol emissions, by modulating atmospheric radiation reaching the surface, have affected oceanic properties such as sea surface temperature (SST), sea surface salinity and heat content (Shi et al., 2023; Dong et al., 2024), which in turn influence ocean heat uptake and heat exchange between basins (Li et al., 2023), and have delayed the formation of the "North Atlantic Warming Hole" (Dagan et al., 2020).

Biomass burning (BMB) emissions, another major partially anthropogenic source of aerosols, have co-evolved with industrial emissions. However, the large-scale climatic impacts of BMB aerosols have received little attention until recently, due in part to incomplete inventories of historical BMB emissions (Hua et al., 2024) and BMB's relatively minor effect on the global mean energy balance (IPCC AR6, 2021). In addition, large uncertainties in BMB-

driven aerosol-cloud interactions, and their dependence on aerosol types has hampered progress (IPCC AR6, 2021). The recent acceleration of human-related wildfire worldwide has prompted renewed scrutiny of the role of BMB emissions in anthropogenic climate change (Cunningham et al., 2024). In particular, it has been demonstrated that BMB emissions reduce time-mean total aerosol radiative forcing (Heyblom et al., 2023), partially mitigating the effect of industrial aerosol emissions on the strength of the Atlantic Meridional Overturning Circulation (AMOC; Allen et al., 2024; Liu et al., 2024) and accelerating externally-forced 20th century warming of the tropical Indian Ocean at a faster speed relative to other tropical ocean basins (Tian et al., 2023). In addition, interannual variations in BMB emissions have been shown to produce a sizeable effect on NH climate via non-linear aerosol-cloud interactions, contributing to high-latitude warming and Arctic sea ice decline in recent decades (Fasullo et al., 2022; DeRepentigny et al. 2022).

Industrial aerosol and BMB emissions are spatially heterogenous and have evolved substantially over time though with different spatiotemporal patterns. Industrial aerosol emissions are primarily located in the NH subtropics and middle latitudes, while BMB emissions mainly occur in the deep tropics and boreal regions (Van Der Werf et al., 2017). From the 1950s-1970s, industrial aerosol emissions increased rapidly over North America and western Europe, followed by marked declines resulting from clean air legislation (e.g., Deser et al., 2020). After the late 1970s, the locus of industrial aerosol emissions shifted to East Asia and South Asia. Following the passage of China's Air Pollution Prevention and Control Action Plan (Zhang et al., 2021), local industrial emissions dropped rapidly particularly after 2013 (Wang et al., 2021), shaping a dipole pattern between East and South Asia (Xiang et al., 2023). Meanwhile, tropical BMB emissions increased substantially over the second half of the 20th century in central Africa, South America and Southeast Asia due to agricultural activities and land use changes (Van Der Werf et al., 2017). Boreal BMB emissions have also risen over the 20th century, particularly in Siberia and parts of Canada (Van Der Werf et al., 2017).

The effect of radiative forcings such as aerosols can be decomposed into atmospheric radiative and ocean-mediated components. These are commonly referred to as "fast" and "slow" responses, respectively, reflecting the timescales over which they appear, where "fast" denotes the response in the absence of significant surface temperature changes and "slow" denotes the surface temperature feedback response (Gregory et al., 2004; Bala et al., 2009). Distinguishing them is important because their drivers emerge on different timescales, and thus

123 the timescale of corresponding responses varies. This decomposition is typically assessed using
124 a parallel set of idealized experiments in which aerosol emissions averaged over a particular
125 time interval of interest are prescribed in both the fully-coupled model and its atmosphere-only
126 component (e.g., Samset et al.,2016; Liu et al., 2018).

127 While such a "time-slice" approach serves as a valuable tool for studying the fundamental
128 physical processes underlying the response to a fixed aerosol emission target, it becomes
129 limited under transient conditions. Given the distinct spatial distributions and temporal
130 evolutions of industrial and BMB aerosols, their varied aerosol types (primarily absorbing
131 carbonous particles for BMB and predominantly scattering particles for industrial aerosols) and
132 location-dependent efficacies (Persad and Caldeira 2018), it is crucial to account for their
133 evolving trajectories when assessing their climate impacts. Under the transient framework, the
134 separation between "fast" and "slow" responses becomes blurred. In particular, the response to
135 time-evolving aerosol emissions in the absence of SST changes (e.g., the radiatively forced
136 contribution) will include a "slow" component by virtue of the fact that aerosol emissions vary
137 slowly through time. Thus, both the atmospheric radiative and ocean-mediated effects of
138 aerosols must be considered on decadal and longer time scales. We emphasize that because
139 aerosol forcing evolves slowly over time, the radiative response is not a purely "fast"
140 adjustment in the classical sense.

141 To date, the climate response to time-evolving patterns of historical industrial, and to a
142 lesser extent BMB, aerosol emissions has been investigated using fully coupled models (e.g.,
143 Deser et al., 2020; Wang and Wen, 2022; Dong et al., 2024). While such studies highlight the
144 importance of accounting for the full spatiotemporal evolution of aerosol emissions, they do
145 not allow for insights into the relative contributions of atmospheric radiative *vs.* ocean-
146 mediated components of response. Moreover, the role of BMB aerosols and their interplay with
147 industrial aerosols has been largely ignored.

148 We address these gaps by employing a novel atmospheric modeling framework to
149 decompose the combined effects of time-varying industrial and BMB aerosol emissions into
150 atmospheric radiative and ocean-mediated components. Specifically, we conduct a suite of
151 experiments with Community Atmosphere Model version 5 (CAM5) forced with time-varying
152 historical aerosol (industrial plus BMB) emissions and associated SST responses individually
153 and in combination, where the aerosol-induced SST changes are derived from the fully coupled
154 Community Earth System Model version 1 (CESM1) Single-Forcing and All-Forcing Large

Ensembles (Kay et al., 2015; Deser et al., 2020). This approach allows us to elucidate the individual roles of evolving atmospheric radiative *vs.* ocean-mediated impacts of industrial and BMB aerosols on historical climate change. A similar methodology has been previously used in the context of idealized 1% per year CO_2 forcing (He and Soden, 2015) and quadrupling of CO_2 concentration (Shaw and Voigt, 2015) experiments, but this is the first time it has been employed for the historical evolution of industrial and BMB aerosols to the best of our knowledge. If adopted in a model intercomparison effort, this framework could also be beneficial for understanding models' structural diversity in aerosol-induced climate change. In addition, this protocol may prove useful for informing dynamical and statistical regional downscaling applications, as it provides large-scale, aerosol-forced signals that can serve as consistent boundary conditions. This consistency is particularly valuable for intercomparisons across models and methods, where isolating the aerosol influence on regional climate remains a key challenge (Nabat et al., 2025).

This study has three aims: 1) To identify the dominant patterns of time-varying aerosol emissions from industrial and BMB sources over the historical period (1920-present); 2) To assess how the dominant patterns of time-evolving aerosol emissions influence precipitation, terrestrial air temperature and the large-scale atmospheric circulation; and 3) To quantify the relative contributions of atmospheric radiative *vs.* ocean-mediated pathways of response. We focus on boreal summer (June-to-August, JJA), when NH monsoon systems and low-level jets drive strong signals, making it a natural season for assessing aerosol impacts particularly at regional scales. Our experimental design is described in Section 2, results are reported in Section 3, and summarized and discussed in Section 4.

2. Data and Methods

a. Model Simulations

We use CAM5 (Neale et al., 2010) coupled to Community Land Model version 4 (CLM4; Lawrence et al., 2011) at a spatial resolution of 1° for our AMIP simulations. CAM5 and CLM4 are the atmospheric and land model components of CESM1, respectively. CAM5 deploys a three-mode modal aerosol scheme (Liu et al., 2012) with prognostic aerosols and includes both the direct and indirect aerosol radiative effects for liquid and ice phase clouds (Morrison and Gettelman 2008). CLM4 includes a biogeochemical model which can prognostically simulate

vegetation changes and a Snow and Ice Aerosol Radiation model which accounts for aerosol's impact on snow cover, as well as its radiative feedback.

At the time we conceived of this study, CESM1 was the only available model version with both Single-Forcing and All-Forcing Large Ensembles: the CESM2 Single-Forcing Large Ensemble (Simpson et al. 2023) had not yet been initiated. Although CESM1 is an older framework, it remains scientifically robust and widely used. Further, it serves as an important benchmark for assessing the impact of horizontal resolution on simulated climate responses due to the advent of the new high-resolution (ocean eddy permitting) version of CESM1 and its All-Forcing Large Ensemble (Chang et al. 2025). We also note that although CESM2(CAM6) employs an updated microphysics scheme with improved representation of ice- and mixed-phase clouds compared to CESM1(CAM5), it overestimates aerosol-induced cooling during the second half of the 20th century as a result of overly strong aerosol-cloud interactions (Zelinka et al. 2020; Flynn and Mauritsen, 2020), which in turn partially compensates for the model's high climate sensitivity (Meehl et al., 2020; Duffy et al., 2026). CESM1(CAM5) has a lower climate sensitivity and weaker aerosol-cloud interactions compared to CESM2(CAM6).

We conducted three sets of AMIP ensembles, termed RAD-AMIP, SST-AMIP and FULL-AMIP (Table 1). Each set has 10 ensemble members and covers the period 1920-2030. For each set, the ensemble members are initialized with a small (order 10^{-14} K) random atmospheric temperature perturbation to create ensemble spread. RAD-AMIP uses time-varying CMIP5 historical (prior to 2006) and Representative Concentration Pathway (RCP) 8.5 (2006 onward) industrial (AER_{indus}) and BMB (from agriculture activities, grass and forest fires) aerosol emissions (Lamarque et al., 2010). All other radiative forcings, as well as SSTs and sea ice concentrations (SICs), are set to their 1920 ensemble-mean seasonal cycles from the 40-member CESM1 "All Forcing" Large Ensemble (ALL). SST-AMIP uses time-varying aerosol-induced SSTs and SICs; all radiative forcings including AER_{indus} and BMB are set to their 1920 ensemble-mean seasonal cycles in ALL. The time-varying aerosol-induced SSTs and SICs are computed from the difference between the ensemble-mean of ALL and the sum of the ensemble-means of the fixed AER_{indus} and fixed BMB CESM1 Single Forcing Large Ensembles following Deser et al. (2020). FULL-AMIP uses the same time-varying aerosol emissions as RAD-AMIP plus the same time-varying SSTs and SICs as SST-AMIP. In the following, we shall refer to the ensemble-mean of the RAD-AMIP simulations as the

217 "radiatively-driven" or "atmospheric radiative" response, and the ensemble-mean of the SST-
218 AMIP simulations as the "SST-driven" or "ocean-mediated" response.

219 We note that although RCP8.5 is an older radiative forcing scenario compared to the Shared
220 Socioeconomic Pathways (SSPs) used in CMIP6, it projects a more realistic evolution of post-
221 2005 Asian aerosol emissions, with a peak during the 2010s followed by a decline through the
222 2020s and 2030s (Takemura et al. 2012; Lund et al. 2019; IPCC AR6; Wang et al. 2024). In
223 contrast, the SSP3-7.0 radiative forcing scenario used for the CESM2 Large Ensemble
224 (Rodgers et al. 2021) erroneously projects a continuous increase in China's aerosol emissions
225 into the 2050s (Xiang et al., 2023). However, both scenarios fail to capture the observed AOD
226 dipole between East and South Asia that has emerged since 2010 as a result of emissions
227 reductions in China and simultaneous increases in India (Xiang et al. 20223).

228

229

230 **Table 1.** CAM5 AMIP experiments and their forcings. Each set of experiments contains 10 ensemble
231 members and covers the period 1920-2030. See text for details.

	RAD-AMIP	**SST-AMIP**	**FULL-AMIP**
Radiative Forcing	Time-varying industrial and BMB aerosol emissions. All other radiative forcings fixed at 1920 levels.	All radiative forcings fixed at 1920 levels.	Time-varying industrial and BMB aerosol emissions. All other radiative forcings fixed at 1920 levels.
SST/SIC Forcing	SST and SIC fixed at 1920 levels.	Time-varying SST and SIC induced by industrial and BMB aerosol emissions.	Time-varying SST and SIC induced by industrial and BMB aerosol emissions.

232

233 *b. AOD and SST patterns*

234 To define the dominant patterns of aerosol radiative forcing in FULL-AMIP, we apply
235 Empirical Orthogonal Function (EOF) analysis to JJA AOD (550nm wavelength) based on
236 low-pass filtered (using 10-year running means) ensemble means from 1930-2030 (we exclude

1920-1929 to minimize the influence of residual memory from ocean initial conditions). The two leading AOD modes account for 94% of AOD variance during 1930-2030 and are thus the focus of our analysis (nearly identical AOD modes are obtained from RAD-AMIP; Fig. S1). To define the aerosol-induced SST patterns, we regress 10-year low-pass filtered ensemble mean SSTs in FULL-AMIP onto the normalized AOD Principal Component (PC) timeseries. The atmospheric responses to the two leading AOD modes are obtained by regressing 10-year low-pass filtered ensemble means of precipitation, sea level pressure (SLP) and land surface air temperature (LSAT) in FULL-AMIP, RAD-AMIP and SST-AMIP onto the normalized AOD PCs. Using aerosol-induced SST PCs in place of AOD PCs yields similar atmospheric regression patterns (Figs. S2 and S3), despite the slight (3-4 year) phase lag between the SST PCs and AOD PCs (Fig. S4); thus, for simplicity, we use AOD PCs throughout this study. Statistical significance of all regression values is assessed using a two-tailed Student's t-test at the 95% confidence level. Our results are not sensitive to the exact choice of running mean filter within the range 6-20 years, nor are they sensitive to the precise selection of start dates (1925-1935) and end dates (2025-2030). We emphasize that the AOD modes identified here should be viewed as diagnostic patterns characterizing the dominant spatio-temporal evolution of global industrial and biomass-burning aerosol emissions over the 20th and early 21st centuries, and may not necessarily represent dynamical modes.

3. Results

a. *Leading modes of AOD variability and associated SST patterns*

The two leading modes of JJA AOD variability show distinctive temporal and spatial characteristics (Fig. 1) and are statistically well separated according to the criterion of North et al. (1982). PC1, which explains 56% of the AOD variance, depicts a pronounced (3 standard deviation) increase from the 1930s-1980s with little change thereafter, while PC2, which explains 38% of the AOD variance, shows more sinusoidal behavior, with a positive trend from about 1935-1975 followed by a steep decline to the early 2020s (Figs. 1a,d). The corresponding AOD spatial pattern associated with PC1 exhibits positive regression values over low latitudes of the Eastern Hemisphere, with regional hotspots in East and South Asia associated with industrial emissions and in tropical South Africa, South America, Indonesia and Malaysia associated with BMB emissions; weak negative values are found in the eastern US and western Europe (Fig. 1b). AOD Mode 2 depicts a zonally-asymmetric NH AOD pattern, with large positive values in the eastern US and western Europe juxtaposed against weaker negative

values in South and East Asia from industrial aerosol emissions and in eastern Siberia from BMB emissions (Fig. 1e). The geographical breakdown of industrial and biomass burning aerosol contributions to the two AOD Modes is shown in Fig. S5 based on CESM1.

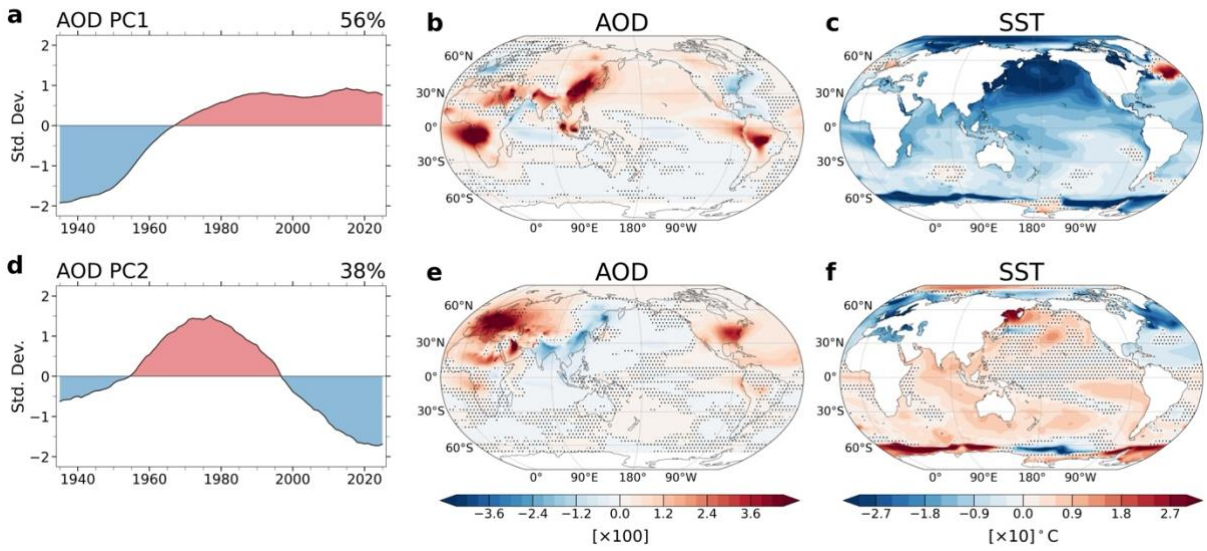

Figure 1. (a,d) Principal Component (PC) time series of Aerosol Optical Depth (AOD) in JJA based on FULL-AMIP. Percent variance explained by Modes 1 and 2 (PC1 and PC2) are given in the upper right. (b,c) Regression of JJA AOD (× 100) and SST (℃ × 10) in FULL-AMIP onto AOD PC1. (e,f) As in (b,c) but for AOD PC2. Statistical significance of all regression values is assessed using a two-tailed Student's t-test with effective degrees of freedom computed according to Bretherton et al. (1999) and applying the False Discovery Rate (FDR) with control level α_{FDR} = 0.05 to measure the field significance of the response (Wilks 2016).

The SST anomalies associated with AOD Mode 1, obtained by regressing ensemble-mean JJA SST anomalies from FULL-AMIP onto AOD PC1, exhibit widespread cooling, as expected from the global increase in AOD (Fig. 1c). The cooling is greatest over the North Pacific and along the sea ice margins of both hemispheres. A strong interhemispheric SST anomaly gradient is evident over the Pacific sector and to a lesser extent the Indian Ocean, likely associated with aerosol emissions over South and East Asia (Hwang et al., 2024). Pronounced SST warming is found in the central subpolar North Atlantic. This may be associated with a strengthening of AMOC and accompanying increase in northward ocean heat transport in response to AOD reductions over eastern North America and Europe (Cai et al., 2006; Delworth & Dixon, 2006; Booth et al., 2012; Menary et al., 2020; Dagan et al., 2020), but local wind-driven processes may also play a role.

293 The SST anomalies associated with AOD Mode 2 are generally weaker than those
294 associated with Mode 1 and depict a strong zonal contrast over the NH with widespread cooling
295 over the North Atlantic and Mediterranean and warming over most of the North Pacific (Fig.
296 1f). The North Atlantic cooling likely arises in response to increased aerosol emissions over
297 the eastern US and Europe (e.g., Undorf et al., 2018a), while the warming in the Pacific and
298 Indian Ocean sectors is presumably a result of reduced AOD over eastern Asia and India (Fig.
299 1f).

300 Investigation of the mechanisms underlying the SST patterns associated with each AOD
301 Mode is beyond the scope of this study, but related analyses may be found in Kang et al. (2021),
302 Shi et al. (2023), Hwang et al. (2024) and Diao et al. (2025), although none considered the
303 combined effects of industrial and BMB aerosols. Here, our interest is in how these aerosol-
304 induced SST patterns impact the atmosphere.

305 *b. Global atmospheric response patterns*

306 We begin by examining the global atmospheric response to combined atmospheric radiative
307 and SST-driven changes associated with each AOD mode. To do this, we regress the FULL-
308 AMIP JJA ensemble-means onto the PC timeseries associated with each AOD Mode.
309 Regression maps of precipitation, SLP and LSAT for AOD Mode 1 are shown in Fig. 2 and for
310 AOD Mode 2 in Fig. 3. Regression maps for associated short-wave surface downward radiative
311 flux (SWSD) under total-sky, clear-sky and cloudy-sky conditions in both modes are given in
312 Fig. 4.

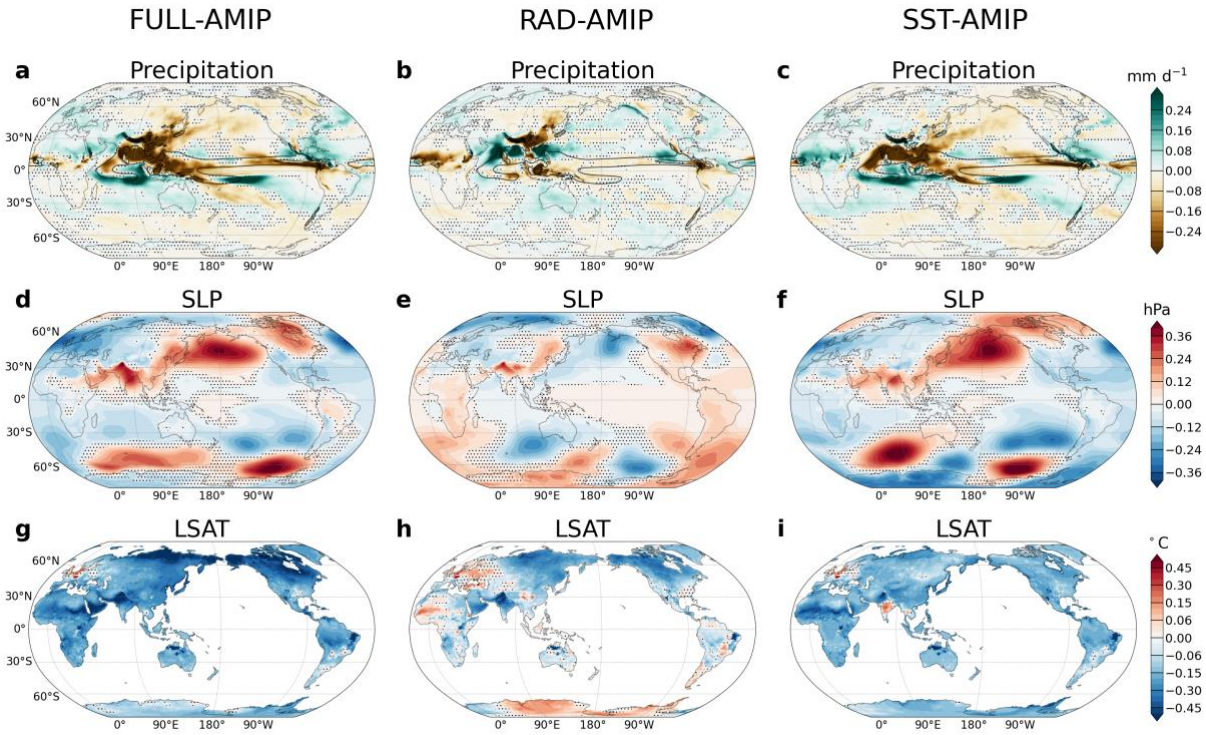

Figure 2. Regressions onto FULL-AMIP AOD PC1 for (a,b,c) precipitation (mm d^{-1}), (d,e,f) sea level pressure (SLP; hPa) and (g,h,i) land surface air temperature (LSAT; °C) in FULL-AMIP, RAD-AMIP and SST-AMIP. Statistical significance of all regression values is assessed using a two-tailed Student's t-test with effective degrees of freedom computed according to Bretherton et al. (1999) and applying the False Discovery Rate (FDR) with control level α_{FDR} = 0.05 to measure the field significance of the response (Wilks 2016).

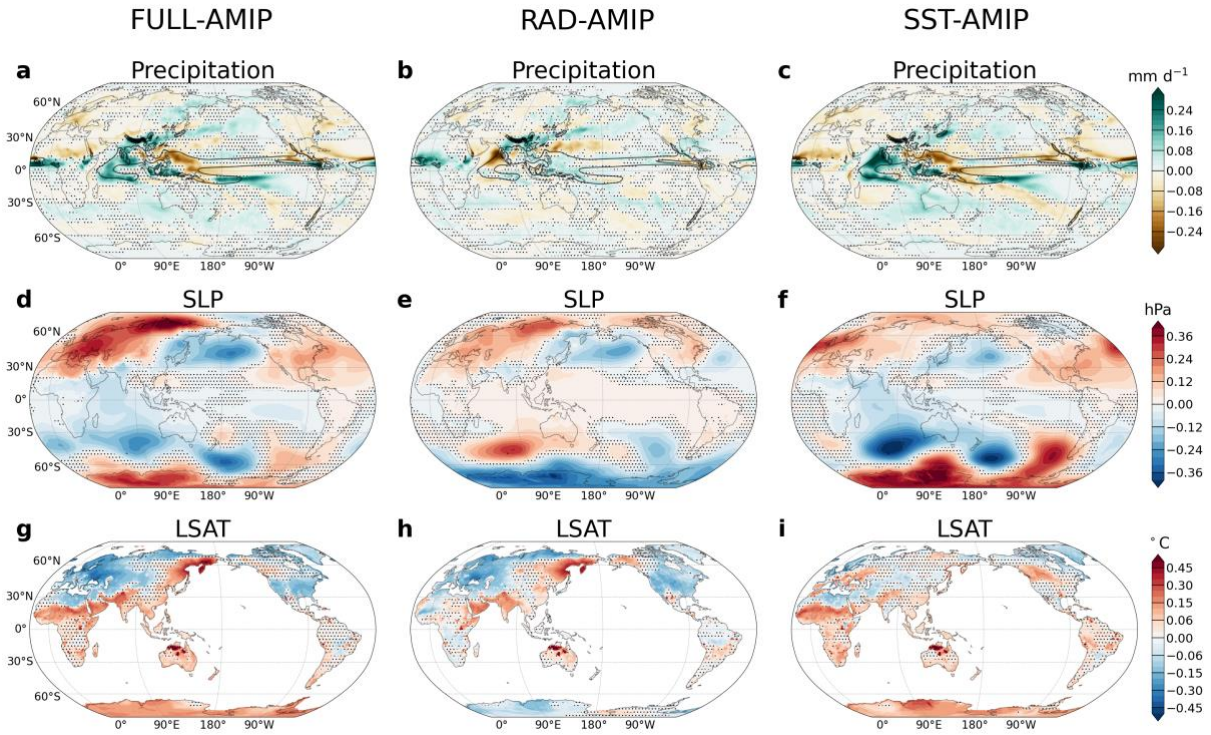

322

323 **Figure 3**. As in Figure 2 but for AOD PC2.

324

325

326

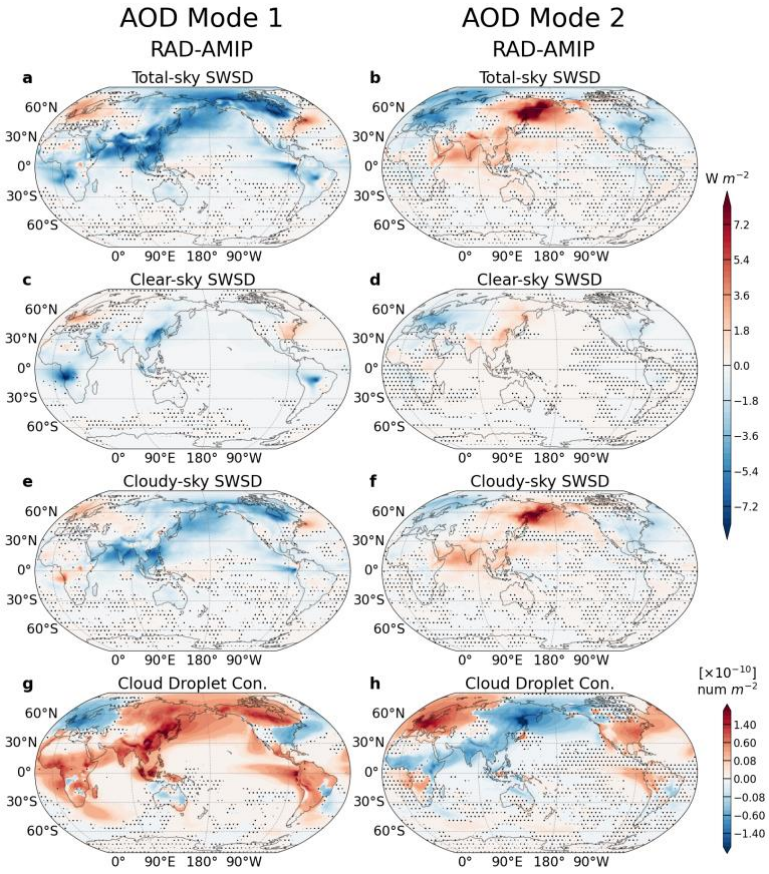

327

328 **Figure 4.** Regressions onto FULL-AMIP AOD PC1 and PC2 for short-wave surface downward (SWSD)
329 radiative flux (W m^{-2}) under (a,b) total-sky, (c,d) clear-sky and (e,f) cloudy-sky conditions, and for (g,h)
330 vertically integrated cloud droplet number concentration (num $m^{-2} \times 10^{-10}$) in RAD-AMIP. Statistical
331 significance of all regression values is assessed using a two-tailed Student's t-test with effective degrees of
332 freedom computed according to Bretherton et al. (1999) and applying the False Discovery Rate (FDR) with
333 control level α_{FDR} = 0.05 to measure the field significance of the response (Wilks 2016).

334

335 Both modes exhibit statistically significant responses that are global in scale. AOD Mode
336 1 features prominent drying over South and East Asia, the northern Indian Ocean and the
337 Maritime Continent, regions proximate to the main centers of AOD increase (Fig. 2a),
338 accompanied by reduction in SWSD (Fig. 4a). Compensating areas of wetting occur directly
339 south of the equator in the Indian Ocean and central Pacific. At higher latitudes, widespread
340 drying is found over the Southern Ocean, the North Pacific, northeastern Asia and western
341 North America, while wetting occurs over the subtropical south Indian and southeast Pacific
342 Oceans, tropical Africa, southern Europe, the Caribbean and parts of the North Atlantic. Areas
343 of drying (wetting) generally correspond to anticyclonic (cyclonic) SLP anomalies, with largest
344 SLP magnitudes in the extra-tropics (Fig. 2d). The prominent positive SLP response over the
345 North Pacific may be due to in part to a remote Rossby wave teleconnection excited by
346 precipitation reductions over the northern Indian Ocean and Southeast Asia (Smith et al., 2016;
347 Dittus et al., 2021) in addition to local SST cooling. Additional detail on the circulation
348 responses over the tropical Indo-Pacific and Southern Hemisphere high latitudes is provided in
349 Section 3c. AOD Mode 1 exhibits widespread terrestrial cooling (Fig. 2g), as expected from
350 the global-scale increase in AOD (Figs. 1a,b) with widespread SWSD reductions (Fig.4a). The
351 strongest cooling is found in boreal regions, likely associated with positive ice/snow albedo
352 feedback. A "cooling hole" is seen over far western Europe, reflecting the local decrease in
353 AOD with positive SWSD values (Fig. 4a). SWSD in FULL-AMIP closely resembles that in
354 RAD-AMIP, whereas SST-driven SWSD responses primarily associated with cloud changes
355 are much weaker. Cloud responses to aerosol strongly affect the SWSD response in remote
356 regions (Fig. 4e), whereas the direct radiative effect dominates locally (Fig. 4c).

357 AOD Mode 2 shows generally weaker responses compared to Mode 1, especially for
358 precipitation and LSAT (Fig. 3). Like Mode 1, Mode 2 AOD increases are generally
359 accompanied by local terrestrial drying and cooling (Figs. 1e and 3g). For example, AOD
360 increases over Europe and the eastern US are accompanied by negative SWSD, primarily
361 driven by aerosol-cloud interactions, whereas AOD decreases over eastern Asia and India

produce the opposite response (Figs. 4b,f,h). Remote precipitation responses are also evident, most prominently in the tropics, including a zonal dipole pattern of drying over the far western Pacific and wetting over the central Indian Ocean, and an increase in precipitation across the equatorial Atlantic. The large-scale SLP response over the extratropical NH is generally opposite in sign between Modes 1 and 2, in keeping with their contrasting NH AOD signatures (Figs. 2d, 3d and 4a,b). However, the tropical and SH SLP response patterns are distinctive between the two AOD modes.

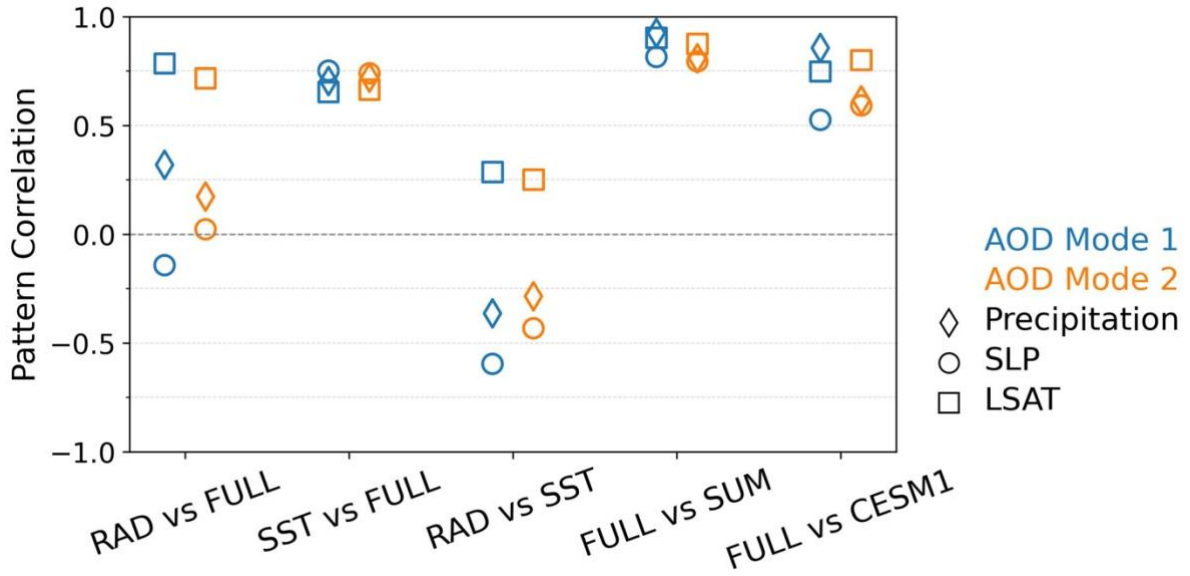

Figure 5. Global pattern correlations of precipitation (diamond), SLP (circle) and LSAT (square) regression maps associated with AOD Mode 1 (blue) and AOD Mode 2 (orange) between different pairs of AMIP simulations. RAD refers to RAD-AMIP, SST refers to SST-AMIP, SUM refers to the sum of RAD-AMIP and SST-AMIP regressions, and FULL refers to FULL-AMIP. Also included are the global pattern correlations between the fully-coupled CESM1 and FULL-AMIP (see text for details).

Next, we assess the relative contributions of atmospheric radiative and ocean-mediated pathways to the atmospheric responses in FULL-AMIP by regressing ensemble-mean fields from RAD-AMIP and SST-AMIP onto the AOD PCs derived from FULL-AMIP. The two pathways produce distinctive and statistically significant global-scale atmospheric responses (Figs. 2 and 3). Comparing to FULL-AMIP, it is readily apparent that the SST-driven response dominates the large-scale patterns of precipitation and SLP response, while radiative forcing tends to oppose SST-induced responses, although the degree of compensation varies with region. On the other hand, radiatively forced and SST-driven responses make comparable contributions to the LSAT response in FULL-AMIP. Quantitatively, the leading role of the

SST-induced response for the precipitation and SLP responses is evidenced by the high pattern correlations (exceeding 0.70) between SST-AMIP and FULL-AMIP, while those between RAD-AMIP and FULL-AMIP are substantially lower (< 0.33; Fig. 5). In contrast, the importance of both radiative forcing and ocean-mediated effect to the patterns of LSAT response is reflected in the comparable magnitudes of spatial correlation between RAD-AMIP and FULL-AMIP and between SST-AMIP and FULL-AMIP (around 0.65 and around 0.75, respectively; Fig. 5). Radiative forcing partially counteracts the SST-driven response for both precipitation and SLP responses, as seen by the modest negative pattern correlations between RAD-AMIP and SST-AMIP (Fig. 5). This negative correlation is particularly pronounced for the SLP response to AOD Mode 1 (-0.60), as is also visually apparent (Figs. 2e,f). However, for LSAT, the correlations between RAD-AMIP and SST-AMIP are weakly positive (Fig. 5).

As mentioned above, the interplay between atmospheric radiative and ocean-mediated pathways depends on the region and quantity of interest. In emission source regions such as East Asia, precipitation responses in both AOD modes are primarily driven by radiative forcing: in Mode 1, AOD increases induce local drying, while AOD decreases in Mode 2 induce local wetting (Figs. 1a,d, 2b and 3b). In contrast, the sign of South Asian precipitation response does not always align with local AOD changes because the SST-driven response dominates. For example, in AOD Mode 1, radiative forcing drives a wetting response despite positive AOD values over South Asia, and this radiatively forced wetting is largely offset by SST-driven drying (Figs. 1a and 2b,c). In the NH mid-latitudes, eastern North America and Europe exhibit robust precipitation and LSAT responses to both AOD modes, driven by a combination of radiatively induced and SST-driven thermodynamic and dynamic mechanisms (Figs. 2b,c and 3b,c). In these regions, LSAT changes reflect compensation between radiatively forced and SST-driven responses, whereas western European precipitation results from the reinforcement of the two pathways of response. Over North America, radiatively and SST-driven precipitation and LSAT responses exhibit distinct patterns, reflecting a tug-of-war between locally and remotely induced circulation influences. For example, in AOD Mode 1, radiative forcing drives a positive North Atlantic Oscillation (NAO)–like response and a slight intensification of the Aleutian Low while SST forcing drives a negative NAO-like response and a marked weakening of the Aleutian Low (Figs. 2e and f). Whether these large-scale circulation responses are triggered by local or remote forcing is hard to determine, warranting further analysis.

In low-emission regions, such as the Sahel, radiatively forced and SST-driven precipitation responses cancel each other, resulting in a muted overall response for both AOD modes (Figs. 2b,c and 3b,c). In contrast, radiatively induced and ocean-mediated SLP responses for Mode 2 are of the same sign over most of the NH and tropics but of opposite polarity over the SH high latitudes (Figs. 3e,f). The NH LSAT response to AOD Mode 1 shows like-signed contributions from radiatively forced and SST-driven responses (Figs. 2h,i), whereas the LSAT response to AOD Mode 2 depicts nearly orthogonal patterns (Figs. 3h,i).

The complex regional interplay between radiatively forced and SST-driven responses raises the question: to what extent are these responses are additive? We address this by comparing the FULL-AMIP regressions with the sum of the RAD-AMIP and SST-AMIP regressions (SUM) in Fig. 6 for Mode 1 and Fig. S6 for Mode 2. Both AOD modes show a large degree of additivity, as evidenced by the overall similarity in pattern and amplitude between SUM and FULL-AMIP. In general, the differences between SUM and FULL-AMIP are relatively small in magnitude, albeit statistically significant, except for SLP at high latitudes where larger discrepancies are found. Pattern correlations between SUM and FULL-AMIP are high (0.79–0.92) for all three variables in both AOD modes (Fig.5).

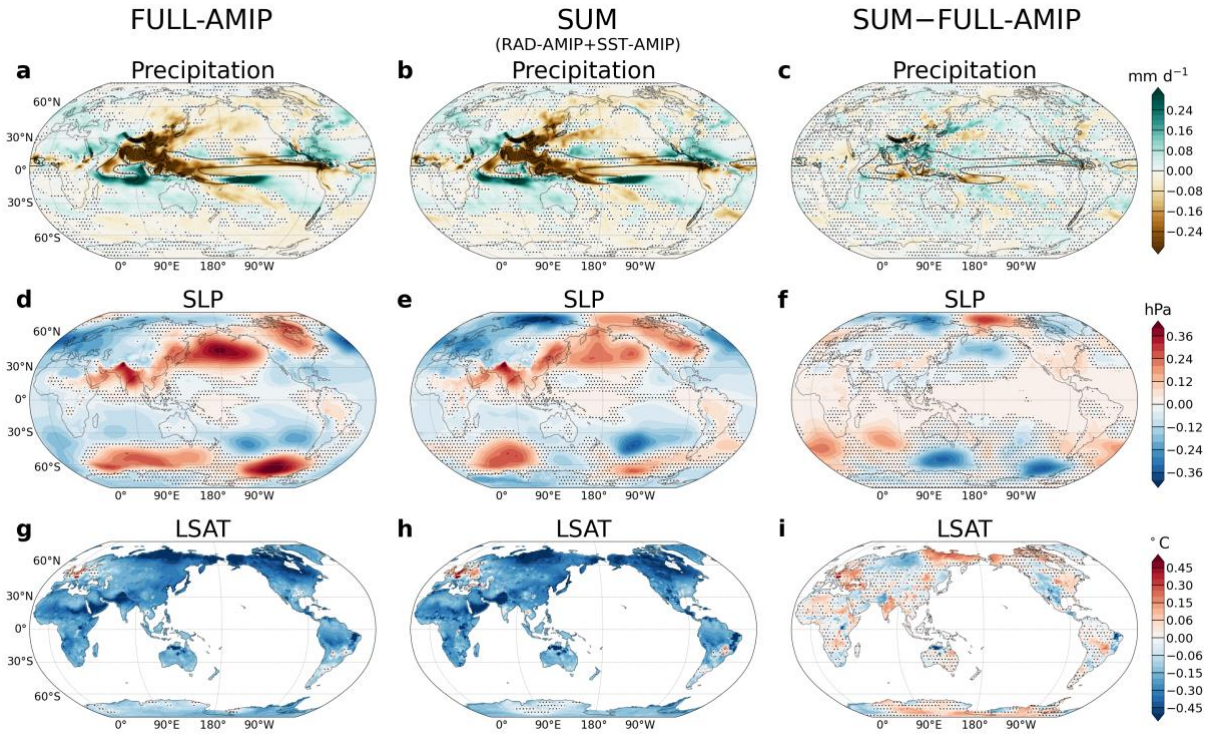

Figure 6. As in Fig. 2 but for additivity analysis based on AOD Mode 1. (a,d,g) FULL-AMIP, (b,e,h) the sum of RAD-AMIP and SST-AMIP (SUM), and (c,f,i) the difference of SUM and FULL-AMIP. Statistical

significance of all regression values is assessed using a two-tailed Student's t-test with effective degrees of freedom computed according to Bretherton et al. (1999) and applying the False Discovery Rate (FDR) with control level α_{FDR} = 0.05 to measure the field significance of the response (Wilks 2016). Black contours on precipitation panels show the climatological 6 mm d^{-1} isopleth.

A separate but related question is: to what extent does the FULL-AMIP response resemble the fully-coupled CESM1 response to industrial and BMB aerosol emissions? Since AMIP simulations necessarily exclude coupled ocean-atmosphere feedbacks by virtue of their design, it is not a given that the response in FULL-AMIP matches that of CESM1(AER_{indus}+BMB). Figure 7 compares the regression maps based on FULL-AMIP with those based on CESM1(AER_{indus}+BMB) for AOD Mode 1; results for Mode 2 are shown in Fig. S7. The precipitation responses are generally similar between the two model configurations (global pattern correlation of 0.86; Fig. 5), with slightly reduced magnitudes in CESM1 compared to FULL-AMIP, particularly over the tropical Indian Ocean and South Asian sector (Fig. 7a,b). In this sector, their difference (CESM1 minus FULL-AMIP) closely resembles the ocean-mediated response pattern but with opposite sign (recall Fig. 2c), indicating that the response in FULL-AMIP (and SST-AMIP) is slightly overestimated due to the lack of air-sea feedbacks. Analogous results are found for the precipitation response to AOD Mode 2 (compare Fig. S7c with Fig. 3c). The SLP responses for AOD Mode 1 show relatively minor differences between CESM1 and FULL-AMIP over the extratropical NH, but considerable discrepancies in magnitude are found over the extratropical SH (Fig. 7d-f), which lower the overall global pattern correlation to 0.56 (Fig. 5). These high latitude circulation disparities may indicate a role for air-sea feedbacks (damping the response over the Pacific and enhancing it over the Indian Ocean: compare with the ocean-mediated response in Fig. 2f) and/or they may stem from the high levels of intrinsic atmospheric variability in austral winter that is not sufficiently eliminated with 10-member ensembles (although our statistical significance test would seem to refute this possibility). Analogous results are found for AOD Mode 2 (Fig. S7 d-f). Finally, the LSAT responses for AOD Mode 1 are generally similar between the two model configurations (global pattern correlation of 0.74; Fig. 5), with a slight overestimate of the cooling in FULL-AMIP compared to CESM1 (except over Antarctica and western Canada), which may be due to neglected damping feedbacks from land-atmosphere coupling (Fig. 7 g-i). The LSAT responses to AOD Mode 2 show only minor discrepancies between the two model configurations (Fig. S7 g-i). In summary, despite the lack of air-sea coupling in the FULL-AMIP protocol, the atmospheric responses to both AOD Modes are

largely similar to CESM1 with exceptions as noted above. This lends confidence to the utility of our AMIP approach for dissecting the fully coupled model's response to time-evolving aerosol emissions.

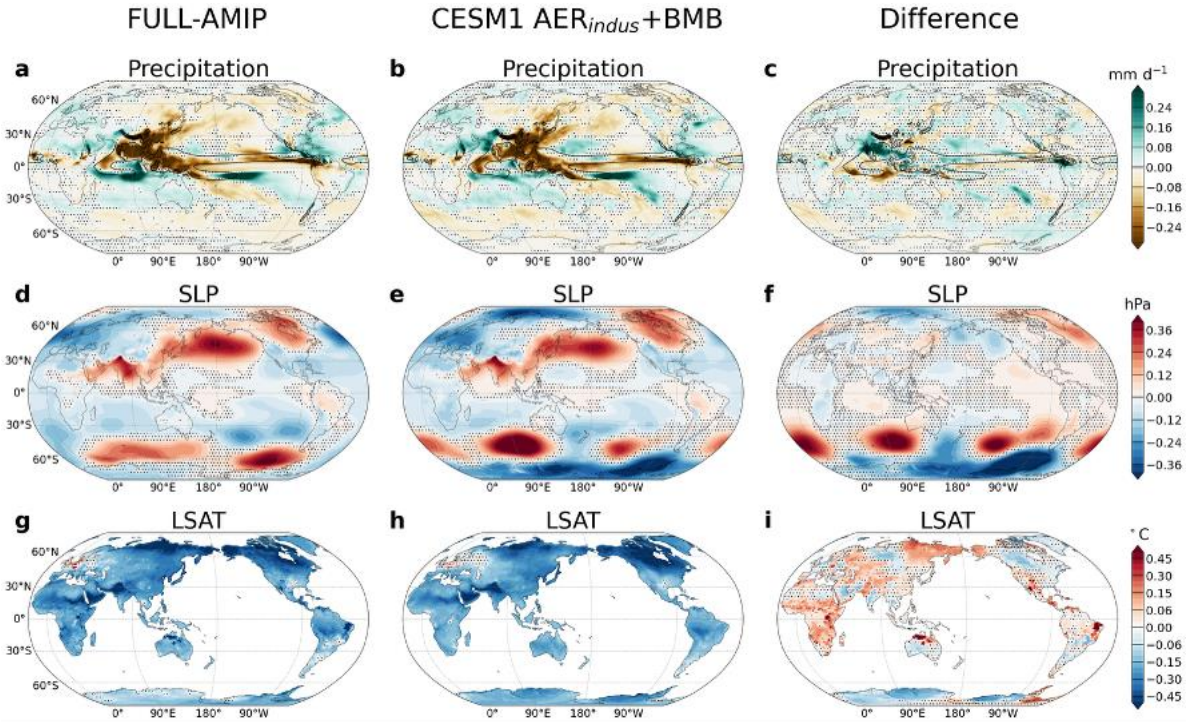

Figure 7. Regressions of Precipitation, SLP and LSAT in FULL-AMIP (left column) and CESM1-AERindus+BMB (middle column) and their difference (CESM1 minus FULL-AMIP; right column) based on AOD PC1 from FULL-AMIP. Statistical significance of all regression values is assessed using a two-tailed Student's t-test with effective degrees of freedom computed according to Bretherton et al. (1999) and applying the False Discovery Rate (FDR) with control level α_{FDR} = 0.05 to measure the field significance of the response (Wilks 2016).

c. *Regional atmospheric response patterns*

The diversity of regional features described above makes it difficult to generalize the relative contributions of atmospheric radiative *vs.* ocean-mediated pathways on aerosol-driven atmospheric responses at the regional scale. To further illustrate this regional variation, we focus here on two areas: the tropical Indo-Pacific sector and Southern Ocean, characterized by distinct response patterns, to demonstrate how radiative forcing originating from regional AOD changes interacts with the SST-driven response to influence the atmosphere locally and remotely.

1) *Tropical Indian-Western Pacific sector*

The pattern of precipitation response to AOD Mode 1 features a distinctive meridional dipole over the tropical Indian-Western Pacific sector in FULL-AMIP (Fig. 8a), indicative of an Asian Summer Monsoon response to shifting historical aerosol emissions that has been a topic of great interest in the literature (Bollasina et al., 2011; Persad et al., 2017; Undorf et al., 2018b; Westervelt et al., 2020). In our simulations, this precipitation dipole response corresponds to a cross-equatorial overturning circulation, with northerly wind anomalies at low-levels and southerly wind anomalies at upper-levels, which feeds anomalous upward motion along 5°-10°S accompanied by anomalous downward motion along 5°-15°N (Figs. 8a,b). This cross-equatorial overturning circulation response results from a subtle interplay between radiatively forced and SST-driven response, which impart different meridional scales and polarities of response. The radiatively forced response exhibits a narrow meridional dipole between the Asian subcontinent from the Tibetan Plateau eastward (27°-30°N) and the northern Indian Ocean-West Pacific (14°-23°N; Figs. 8c,d), while the SST-driven response displays a broader latitudinal dipole structure between the northern (5°-20°N) and southern (5°-12°S) portions of the Indian Ocean (Figs. 8e,f). The radiatively forced and SST-driven responses are offsetting over the northern Indian Ocean. As a result, the response in FULL-AMIP shows a hybrid structure, with characteristics of both the SST-driven response (i.e., the broad cross-equatorial dipole, albeit substantially weaker in its northern lobe) and the radiatively forced response (i.e., the narrow meridional dipole over the Tibetan Plateau extending eastward).

The SST-driven precipitation dipole response (Figs. 2a, 8a) likely results from the enhanced meridional temperature gradient over the Indian Ocean (i.e., stronger cooling north of the equator than south; Li et al., 2020), although the pronounced large-scale cooling of the North Pacific may also play a role in displacing the rain belt southward (recall Fig. 1c). Conversely, the radiatively forced precipitation dipole response is likely driven by locally induced drying and subsidence from aerosol emissions over East Asia, with compensating upward motion over the Arabian Sea, Bay of Bengal and the South China Sea (Bollasina et al., 2011; Persad et al., 2017; Westervelt et al., 2020); enhanced cooling over land may also contribute to ascent over the nearby seas.

Both aerosol direct and indirect radiative effects contribute to enhanced cooling over Southeast Asia in RAD-AMIP, as seen from the SWSD under clear and cloudy skies, respectively (Figs. 4a,c,e). Aerosol direct effects (e.g., clear-sky SWSD) dominate locally over the aerosol emission source regions (Fig. 4c), while aerosol indirect effects (e.g., cloudy-sky

SWSD and associated increase in cloud droplet number concentration) prevail in adjacent regions including the northern Indian Ocean (Figs. 4e,g). Note that the reduction in cloudy-sky SWSD over the northern Indian Ocean and western North Pacific in RAD-AMIP would act to cool the underlying SSTs if the ocean were allowed to respond, consistent with the negative SST anomalies found in SST-AMIP. In SST-AMIP, adiabatic heating associated with the descending branch of the overturning circulation response over the northern Indian Ocean (Figs. 8e,f) reduces cloud cover and allows more insolation to reach the surface (not shown), warming the adjacent Indian Peninsula and parts of central Mainland Southeast Asia (Fig. 2i). However, this warming effect is overwhelmed by radiatively forced cooling (Fig. 2h), resulting in net cooling over these regions in FULL-AMIP (Fig. 2g).

The relative role of RAD-AMIP (i.e. atmosphere radiative effects) *vs.* SST-AMIP (i.e. ocean-mediated effects) provides valuable insight on the relative importance of in-situ *vs.* large scale responses to aerosol changes in driving summertime rainfall trends in this region, which has been a topic of substantial debate (Bollasina et al., 2011; Persad et al. 2017; Dong et al;, 2019; Li et al., 2018; Wang et al., 2019; Westervelt et al. 2020). AOD Mode 1 captures prevailing northly wind anomalies and precipitation reductions over Asian Summer Monsoon land regions, indicating a weakening of Asian Summer Monsoon (Li et al., 2018; Wang et al., 2019). The SST-driven cross-equatorial dipole circulation accounts for the precipitation response over the central to southern Indian Peninsula and adjacent oceans. In contrast, East Asian Monsoon weakening arises primarily from a local radiatively dominated response, with subsiding motion accompanied by terrestrial cooling and positive SLP anomalies, that in turn suppresses ascending motion over the Tibetan Plateau extending eastward. These results suggest that historical South Asian Summer Monsoon weakening reflects effects of East Asian aerosols (Shawki et al, 2018) in Mode 1 here, given the importance of the ocean-mediated response. But, when not decomposed by mode, the full response of South Asian Summer Monsoon to aerosols likely includes contributions from other remote sources such as Europe and North America (Bollasina et al., 2014; Undorf et al., 2018b). In contrast, East Asian Monsoon weakening is primarily attributable to local aerosols through the atmospheric radiative pathway. Given that the total response of East Asian Summer Monsoon precipitation to aerosols is dominated by Mode 1 and partially compensated by Mode 2, in keeping with their opposite-signed local AOD anomalies (Figs. 1b,d and 2a,3a), this indicates that historical East Asian Summer Monsoon weaking and associated land drying is likely dominated by local aerosols through the atmospheric radiative pathway.

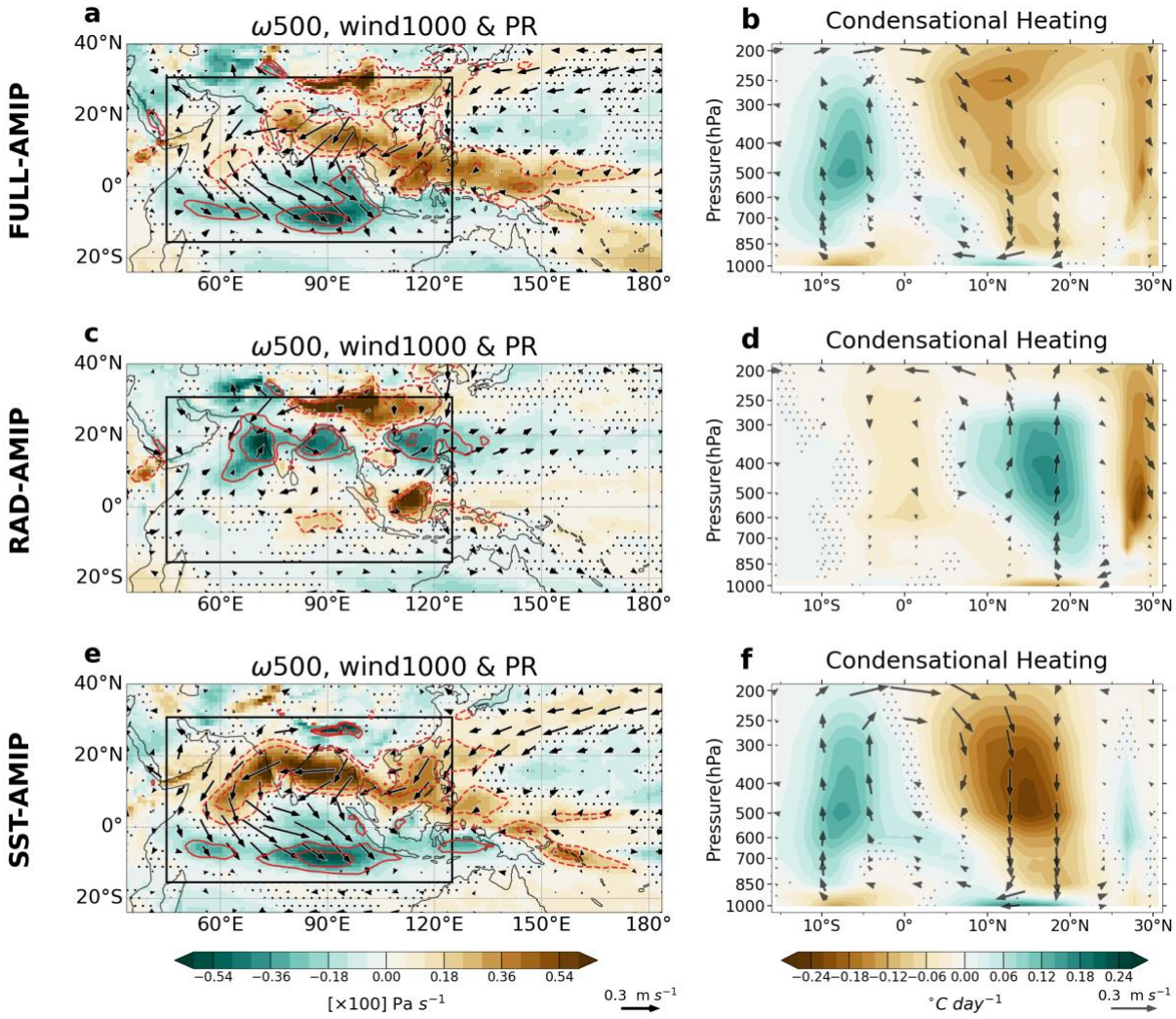

Figure 8. AOD Mode 1 tropical Indo-Pacific response of (a,c,e) 500hPa ω ($Pa\ s^{-1} \times 100$; color shading), 1000 hPa vector wind (m s^{-1}; reference vector in lower right) and precipitation (mm day^{-1}; red contours), and (b,d,f) zonally-averaged (45°-125°E) condensational heating (℃ d^{-1}; color shading) and v, ω vectors (v: m s^{-1}, reference vector in lower right; ω: $Pa\ s^{-1} \times 50$) in FULL-AMIP, RAD-AMIP and SST-AMIP regressed onto AOD PC1. Red contours in (a,c,e) show precipitation regression slopes, starting from ±0.2 mm d^{-1} and contoured at ±0.2 mm day^{-1} intervals, with solid lines for positive values and dashed lines for negative values. Statistical significance of all regression values is assessed using a two-tailed Student's t-test with effective degrees of freedom computed according to Bretherton et al. (1999) and applying the False Discovery Rate (FDR) with control level α_{FDR} = 0.05 to measure the field significance of the response (Wilks 2016). Horizontal wind magnitudes < 0.01 m s^{-1} are omitted for clarity.

2) Southern Hemisphere Circulation

A notable aspect of AOD Mode 1 is the SLP response pattern over the SH, which resembles a Rossby wave train in both RAD-AMIP and SST-AMIP, but with opposite sign (Figs. 2e,f). In contrast, FULL-AMIP shows a zonally symmetric structure over the SH extra tropics, with positive (negative) SLP anomalies at high (middle) latitudes (Fig. 2d). SH circulation trends have been linked to anomalous heating in the tropics which can trigger tropical–extratropical teleconnections (Berbery et al. 1992; Hoskins and Ambrizzi 1993). Guided by this theory, we

pose an open question: can low-latitude aerosols, particularly central African BMB emissions given their geographic proximity, modulate SH circulation through teleconnection dynamics via an atmospheric radiative pathway, and how does this compare with teleconnections driven by the ocean-mediated response? These SH anomalous upper-level circulations can potentially influence Australian precipitation (Ashok et al., 2003; Cai et al., 2011) and Antarctic climate through the Tropical-Antarctic teleconnection (Ding and Steig, 2013; Li et al., 2021).

To understand the origin of the Rossby wave train responses, we examine the upper-level circulation and its connection to tropical precipitation. The 250 hPa meridional wind (V250) anomalies clearly delineate poleward propagating Rossby wave trains of opposite sign in response to the radiatively forced and SST-driven responses, which appear to originate in the Gulf of Guinea and propagate southeastward over the southern Indian Ocean and into the Pacific sector of the Southern Ocean (Figs. 9c,e). The SST-driven Rossby wave train takes a slightly more poleward route than the radiatively forced one. FULL-AMIP lacks a poleward-propagating Rossby wave signature due to the large degree of cancellation between RAD- and SST-AMIP (Fig. 8a). Instead, FULL-AMIP shows a zonally-oriented V250 wave train emanating from the tip of South Africa and extending eastward across the Indian and Pacific Oceans along the latitude (30°S) of the subtropical jet maximum, which acts as a wave guide (Fig. 9b).

Both the radiatively forced and SST-driven V250 Rossby wave trains appear to be initiated by tropical precipitation and associated diabatic heating anomalies over Africa and the Indian Ocean (Figs. 9d,f). In SST-AMIP, upper-level divergence associated with increased precipitation over the Sahel produces the negative (northerly) V250 anomaly centered over the Gulf of Guinea (Fig. 9f). As the anomalous northerly divergent winds cross the equatorward flank of the climatological subtropical westerly jet, it generates a negative Rossby wave source (RWS) to the west of South Africa, which triggers a downstream Rossby Wave response (Fig. 9f). Increased precipitation in the tropical Indian Ocean along 10°S may also act to reinforce the Rossby Wave response. These results are consistent with previous studies which show the critical role of the subtropical jet in amplifying upper-level circulation anomalies emanating from tropical heating (Berbery et al. 1992; Hoskins and Ambrizzi 1993; Li et al., 2015) and serving as a waveguide into the SH extra tropics (Gillett et al. 2021). In RAD-AMIP, upper-level convergence associated with diminished precipitation over the Sahel produces the positive (southerly) V250 anomaly centered over the Gulf of Guinea (Fig. 9d). Unlike SST-

AMIP however, RAD-AMIP shows a large AOD increase over the African Democratic Republic associated with local BMB emissions (recall Fig. 1b). The resulting anomalous heat source from absorbing BMB aerosols is balanced by adiabatic ascent, accompanied by upper-level divergence (Fig. 9d). The divergent V250 anomaly crossing the equatorward flank of the subtropical jet over the southwestern Indian Ocean generates a positive RWS anomaly, which in turn triggers the downstream Rossby wave train response (Fig. 9d). We emphasize that the mechanistic explanations offered above remain speculative and warrant further investigation using targeted experiments with simpler (e.g., linear barotropic) models forced with regional heating and vorticity anomalies.

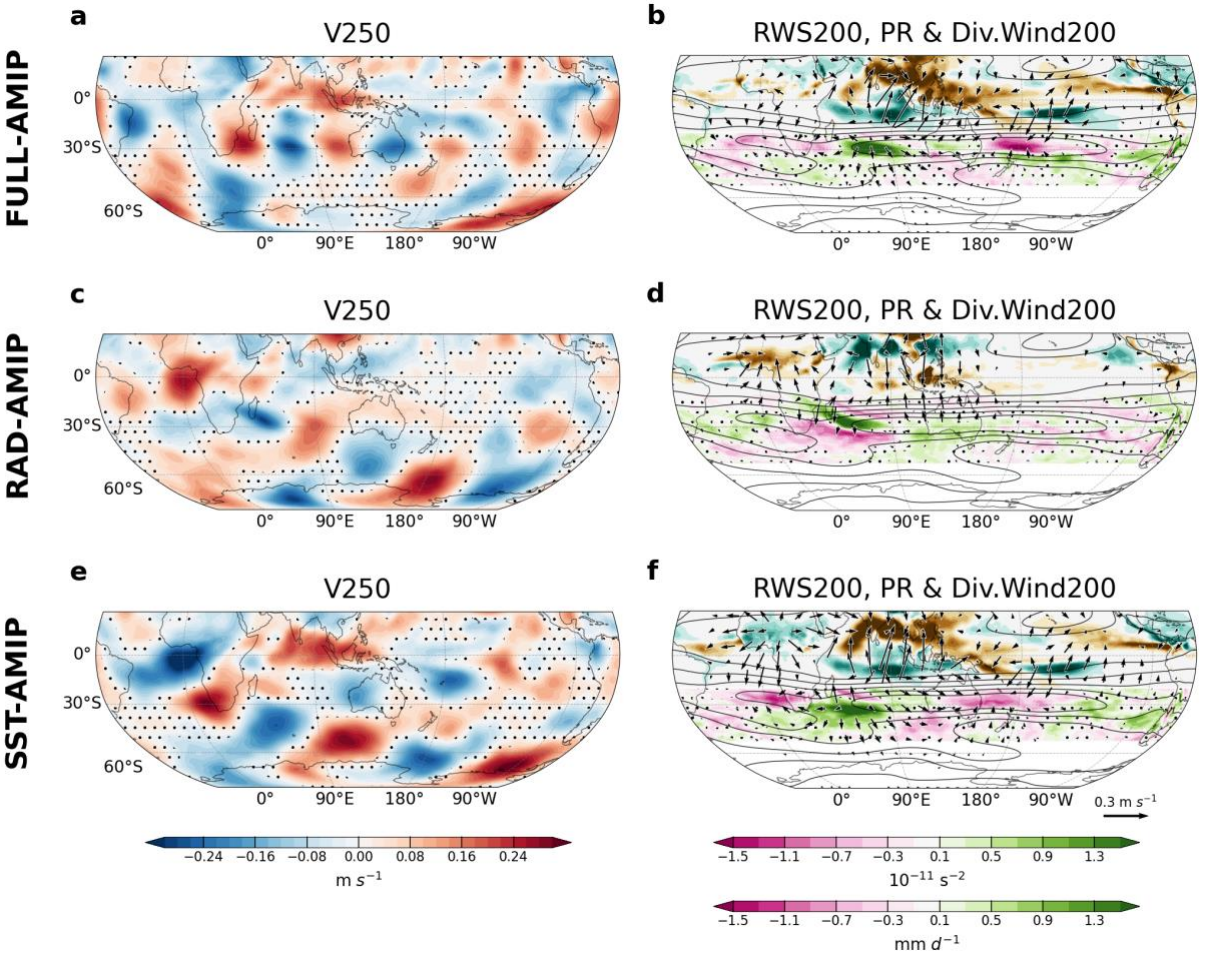

Figure 9. AOD Mode 1 Southern Hemisphere response of (a,c,e) 250 hPa meridional wind (V250; m s^{-1}) and (b,d,f) 200 hPa Rossby wave source (RWS200; pink-green color bar; 10^{-11} s^{-2}), precipitation (PR; green-brown color bar; mm d^{-1}) and 200 hPa divergent wind vector (m s^{-1}; reference vector in lower right) regressed onto AOD PC1 in FULL-AMIP, RAD-AMIP and SST-AMIP. For clarity, RWS200 (precipitation) regressions are only shown in the latitude band 52°-20°S (19°S-26°N) in FULL-AMIP and SST-AMIP and 52°-6°S (6°S-26°N) in RAD-AMIP; wind vectors with magnitudes < 0.03 m s^{-1} are omitted. The climatological 250hPa zonal wind is contoured in black (contour interval = 10 m s^{-1} from 5-45 m s^{-1}).

Statistical significance of all regression values is assessed using a two-tailed Student's t-test with effective degrees of freedom computed according to Bretherton et al. (1999) and applying the False Discovery Rate (FDR) with control level $\alpha_{FDR} = 0.05$ to measure the field significance of the response (Wilks 2016).

4. Summary and Discussion

There is increasing recognition that the global climate response to anthropogenic aerosols is sensitive to the pattern of regional emissions, which has shifted over time, necessitating a broader view of their role in historical climate change (Persad and Caldeira, 2018; Deser et al. 2020; Kang et al. 2021; Wang and Wen, 2022; Persad, 2023; Shi et al. 2023; Dong et al. 2024; Diao et al. 2025). In particular, two distinct modes of AOD variability from industrial sources have been identified over the past century: the "global increase mode" primarily associated with Asian emissions but modulated by emissions over North America and Europe, and the "shift mode" reflecting a zonal redistribution of NH emissions between the western and eastern hemispheres (Kang et al. 2021; Wang and Wen, 2022; Shi et al. 2023; Dong et al. 2024). These AOD modes can produce synergistic and competing effects with GHGs depending on the period of interest, complicating detection and attribution efforts (Dong et al. 2024). The dynamical mechanisms underpinning the global response to the "global increase" and "shift" modes of industrial aerosol emissions have been investigated in idealized coupled modeling studies, revealing the importance of both atmospheric and oceanic processes (Kang et al. 2021; Wang and Wen, 2022; Shi et al. 2023; Diao et al. 2025). However, non-linear interactions between aerosol emissions in different regions complicates a full understanding and interpretation of the combined effects of the two AOD modes (Diao et al. 2025).

In this study, we provide additional insight into the pathways by which time-evolving anthropogenic aerosols from combined industrial and BMB sources over the past century influence boreal summer (JJA) climate. In particular, we utilize a novel atmospheric modeling framework to separate the atmospheric radiative and ocean-mediated pathways of response. We partition the full spatio-temporal evolution of historical aerosol emissions into two leading diagnostic patterns based on EOF analysis and elucidate the response pathways for each.

AOD variations arising from industrial and BMB sources can be decomposed into two leading EOFs, which together explain 94% of global JJA AOD variance during 1930-2030 (56% for Mode 1 and 38% for Mode 2). AOD Mode 1 increases monotonically over the first half of the record with little change thereafter, in contrast to Mode 2 which exhibits sinusoidal

behavior, with a positive trend from the mid-1930s to the mid-1970s followed by a steep decline to the early 2020s. Mode 1 features positive AOD anomalies at low latitudes, with regional hotspots in East and South Asia associated with industrial emissions and in tropical South Africa, South America, Indonesia and Malaysia associated with BMB emissions, accompanied by weak negative AOD anomalies in western Europe and the eastern US. While Mode 2 is characterized by large positive AOD values in western Europe and the eastern US, juxtaposed against weaker negative values in South and East Asia and eastern Siberia. The two AOD modes are broadly consistent with the "global increase" and "shift" modes reported in prior studies that considered industrial aerosols alone (e.g., Wen and Wang, 2022; Shi et al., 2023; Dong et al., 2024).

The ocean-mediated pathway tends to dominate the global large-scale circulation and precipitation responses to both AOD Modes, with offsetting contributions from the atmospheric radiative pathway. However, the interplay between the two pathways is complex and regionally dependent, making it difficult to generalize. In contrast, radiative forcing and SST-driven influences are comparable for the NH LSAT response to Mode 1 (low-latitude aerosols), whereas for Mode 2 radiative forcing dominates. This suggests that low-latitude aerosols can locally perturb terrestrial air temperatures through both pathways, making them efficient in driving regional changes. In contrast, mid-latitude aerosols primarily drive in-situ surface air temperature changes through the atmospheric radiative pathway. Although mid-latitude aerosols exert weaker local impacts, they have high efficacy in driving remote surface air temperature responses, including contributing to global mean surface air temperature (Shindell and Faluvegi, 2009; Persad and Caldeira, 2018).

The tropical Indo-Pacific and SH circulation responses to AOD Mode 1 exemplify how low-latitude aerosols exert both local and remote influences via atmospheric radiative and SST-induced effects. The tropical Indo-Pacific sector displays a distinctive meridional dipole response in precipitation and tropospheric overturning circulation. The latitudinal structure of this response represents a hybrid between the broad cross-equatorial scale resulting from the ocean-mediated pathway associated with remote and local aerosols (Bollasina et al., 2014; Undorf et al., 2018b), and the narrower NH dipolar pattern driven by the atmospheric radiative pathway, which likely reflects the influence of aerosols from adjacent sources (Fig. 5 in Persad, 2023). In the SH, both the radiatively forced and SST-driven responses produce poleward-propagating Rossby wave trains emanating from the tropics into the extratropics, but with

opposite sign. Their largely canceling responses appear to be initiated by tropical diabatic heating anomalies from convection changes over the Sahel and tropical Indian Ocean in response to remote industrial aerosols, along with adiabatic heating anomalies associated with central Africa BMB aerosols in the atmospheric radiative case. These results suggest a potential aerosol-driven tropical–extratropical teleconnection in the SH, though confirmation with linear models or targeted experiments is needed.

Under the transient framework, we showed that the interplay of atmospheric radiative and ocean-mediated effects is neither uniform nor stationary. Radiative effects can exert not only short-lived adjustments but also persistent, decadal-scale influences. This blurs the conventional distinction between "fast" and "slow" responses to radiative forcing, as long-term evolving radiative forcing itself may encompass a slow component (i.e., the radiative response is not a purely "fast" adjustment in the classical sense). With aerosol emissions expected to decline, and clean air legislation already enacted in some countries, it is critical to account for both atmospheric radiative and ocean-mediated components of aerosol effects when predicting regional hydroclimate and risks such as heat extremes, given the mobility and geography-dependent nature of their nuanced interplay.

Much remains to be understood about the mechanisms underlying the atmospheric radiative and ocean-mediated pathways of response to the two AOD Modes documented here, including the relative contributions of local *vs.* remote aerosol emissions and their mode dependence, warranting further analysis of our experiments. Our study has utilized one climate model (CESM1) and one (CMIP5) representation of historical time-evolving industrial and biomass burning aerosols, both of which have known strengths and shortcomings (e.g., Holland et al. 2024). Repeating our approach with other models and updated aerosol emissions inventories (such as the CMIP6 SSPs) would be a useful next step for addressing structural and forcing uncertainty. In particular, different microphysical schemes and associated aerosol-cloud interactions may alter the simulated magnitudes and patterns of aerosol-induced effects, including the SST responses which may bias the ocean-mediated atmospheric response to aerosol forcing. Models with improved representation of aerosol microphysical processes and aerosol-cloud interactions, enhanced vertical and horizontal resolution, and interactive wildfire capabilities, may be especially valuable in this regard. Applying our protocol to regional aerosol forcing experiments such as those conducted as part of the Regional Aerosol Model Intercomparison Project (Wilcox et al. 2023) may yield additional mechanistic insights,

although non-linear interactions between forcings in different regions may complicate the picture (Diao et al. 2025). Additionally, addressing the seasonal dependence of the AOD modes and the responses they elicit would be a worthwhile next step.

Looking forward, anthropogenic aerosol emissions are expected to undergo substantial changes. With continued air quality regulation in Asia and growing industrial activity in tropical regions, the center of aerosol emissions may shift to South Asia, South America, and Africa, though the timing of this transition remains uncertain (Scholten et al., 2024). This shift is especially concerning given the hydrological sensitivity of the tropics and its ability to influence climate worldwide via teleconnections (Smith et al., 2016; Dittus, et al., 2021; Liu et al., 2024). Given the critical role of anthropogenic aerosols in shaping historical changes in regional precipitation over densely populated areas (White et al. 2026), there is an essential need to incorporate information on anticipated near-term and long-term changes in both industrial and biomass burning aerosol emissions into climate projections and risk assessments (Persad et al., 2023). Importantly, understanding the physical pathways by which aerosols impact global climate would not only improve our interpretation of historical climate trends, but also enhance the reliability of future projections in a world increasingly shaped by GHGs and shifting aerosol regimes.

Acknowledgements

We thank both anonymous Reviewers for their thoughtful and constructive comments and suggestions which led to improvements in this work. This work was supported by funding from the National Science Foundation (NSF) under award #2235177. This material and the CESM project are based on work supported by the National Center for Atmospheric Research (NCAR), which is a major facility sponsored by the NSF under Cooperative Agreement 1852977. Computations and data storage resources were provided by the Computational and Information Systems Laboratory (CISL) at NCAR.

Data Availability Statement.

The CESM1 CAM5 AMIP single-forcing experiment data will be made available through a NCAR GLOBUS guest collection upon publication. The CESM1 Large Ensemble simulations used in this study are available from

http://www.cesm.ucar.edu/experiments/cesm1.1/LE/#single-forcing and http://www.cesm.ucar.edu/projects/community-projects/LENS.

REFERENCES

Allen, R. J., A. T. Evan, and B. B. B. Booth, 2015: Interhemispheric Aerosol Radiative Forcing and Tropical Precipitation Shifts during the Late Twentieth Century. J. Climate, 28, 8219–8246, https://doi.org/10.1175/JCLI-D-15-0148.1.

Allen, R.J., Vega, C., Yao, E., and Liu, W., 2024: Impact of industrial versus biomass burning aerosols on the Atlantic Meridional Overturning Circulation. npj Climate and Atmospheric Science, 7(1), p.58, https://doi.org/10.1038/s41612-024-00602-8.

Ashok, K., Guan, Z. and Yamagata, T., 2003: Influence of the Indian Ocean Dipole on the Australian winter rainfall, Geophys. Res. Lett., 30, 1821, doi:10.1029/2003GL017926, 15.

Bala, G., Caldeira, K., and Nemani, R., 2010: Fast versus slow response in climate change: implications for the global hydrological cycle. *Climate dynamics*, *35*, pp.423-434, https://doi.org/10.1007/s00382-009-0583-y.

Berbery, E. H., J. Nogués-Paegle, and J. D. Horel, 1992: Wavelike Southern Hemisphere Extratropical Teleconnections. *J. Atmos. Sci.*, 49, 155–177, https://doi.org/10.1175/1520-0469(1992)049<0155:WSHET>2.0.CO;2.

Bollasina, M.A., Ming, Y. and Ramaswamy, V., 2011: Anthropogenic aerosols and the weakening of the South Asian summer monsoon. Science, 334(6055), pp.502-505, DOI:10.1126/science.1204994

Bollasina, M.A., Ming, Y., Ramaswamy, V., Schwarzkopf, M.D. and Naik, V., 2014: Contribution of local and remote anthropogenic aerosols to the twentieth century weakening of the South Asian Monsoon. Geophys. Res. Lett., 41, 680–687, doi:10.1002/2013GL058183.

Booth, B.B., and Coauthors, 2012: Aerosols implicated as a prime driver of twentieth-century North Atlantic climate variability. *Nature*, *484*(7393), pp.228-232, https://doi.org/10.1038/nature10946.

781 Bretherton, C. S., M. Widmann, V. P. Dymnikov, J. M. Wallace, and I. Bladé, 1999: The
782 Effective Number of Spatial Degrees of Freedom of a Time-Varying Field. J. Climate, 12,
783 1990–2009, https://doi.org/10.1175/1520-0442(1999)012<1990:TENOSD>2.0.CO;2.

784 Cai, W., D. Bi, J. Church, T. Cowan, M. Dix, and L. Rotstayn, 2006*:* Pan-oceanic response to
785 increasing anthropogenic aerosols: Impacts on the Southern Hemisphere oceanic
786 circulation. *Geophys. Res. Lett.*, *33*, L21707, doi:10.1029/2006GL027513.

787 Cai, W., P. van Rensch, T. Cowan, and H. H. Hendon, 2011: Teleconnection Pathways of
788 ENSO and the IOD and the Mechanisms for Impacts on Australian Rainfall. J. Climate,
789 24, 3910–3923, https://doi.org/10.1175/2011JCLI4129.1.

790 Chang, P., D. Fu, X. Liu, F.. Castruccio, A.. Prein, G. Danabasoglu, X. Wang, J. Bacmeister,
791 Q. Zhang, N. Rosenbloom, T. King, and S.. Bates, 2025: Future extreme precipitation
792 amplified by intensified mesoscale moisture convergence. *Nature Geoscience*. DOI:
793 10.1038/s41561-025-01859-1.

794 Chemke, R. and Coumou, D., 2024: Human influence on the recent weakening of storm
795 tracks in boreal summer. *npj Climate and Atmospheric Science*, *7*(1), p.86,
796 https://doi.org/10.1038/s41612-024-00640-2.

797 Cunningham, C.X., Williamson, G.J., and Bowman, D.M., 2024: Increasing frequency and
798 intensity of the most extreme wildfires on Earth. Nature ecology & evolution, 8(8),
799 pp.1420-1425, https://doi.org/10.1038/s41559-024-02452-2.

800 Dagan, G., Stier, P., and Watson-Parris, D., 2020: Aerosol forcing masks and delays the
801 formation of the North Atlantic warming hole by three decades. *Geophysical Research*
802 *Letters*, 47(22), p.e2020GL090778, https://doi.org/10.1029/2020GL090778.

803 Delworth, T. L., and K. W. Dixon, 2006*:* Have anthropogenic aerosols delayed a greenhouse
804 gas-induced weakening of the North Atlantic thermohaline circulation? *Geophys. Res.*
805 *Lett.,*33, L02606, doi:10.1029/2005GL024980.

806 DeRepentigny, P., Jahn, A., Holland, M.M., Kay, J.E., Fasullo, J., Lamarque, J.F., Tilmes, S.,
807 Hannay, C., Mills, M.J., Bailey, D.A., and Barrett, A.P., 2022: Enhanced simulated early
808 21st century Arctic sea ice loss due to CMIP6 biomass burning emissions. *Science*
809 *Advances*, *8*(30), p.eabo2405, DOI:10.1126/sciadv.abo2405.

Deser, C., and Coauthors, 2020: Isolating the Evolving Contributions of Anthropogenic Aerosols and Greenhouse Gases: A New CESM1 Large Ensemble Community Resource. *J. Climate*, 33, 7835–7858, https://doi.org/10.1175/JCLI-D-20-0123.1.

Diao, C., Xu, Y., Hu, A., and Wang, Z., 2025: Contrasting the roles of regional anthropogenic aerosols from the western and eastern hemispheres in driving the 1980-2020 Pacific multi-decadal variations. *Atmospheric Chemistry and Physics*, *25*(4), pp.2167-2180, https://doi.org/10.5194/acp-25-2167-2025.

Ding, Q., and E. J. Steig, 2013: Temperature Change on the Antarctic Peninsula Linked to the Tropical Pacific. J. Climate, 26, 7570–7585, https://doi.org/10.1175/JCLI-D-12-00729.1.

Dittus, A.J., Hawkins, E., Robson, J.I., Smith, D.M., and Wilcox, L.J., 2021: Drivers of recent North Pacific decadal variability: The role of aerosol forcing. *Earth's Future*, *9*(12), p.e2021EF002249, https://doi.org/10.1029/2021EF002249.

Dong, B., Sutton, R.T., Shaffrey, L. and Harvey, B., 2022: Recent decadal weakening of the summer Eurasian westerly jet attributable to anthropogenic aerosol emissions. Nature Communications, 13(1), p.1148, https://doi.org/10.1038/s41467-022-28816-5.

Dong, B., Wilcox, L.J., Highwood, E.J. *et al.,* 2019: Impacts of recent decadal changes in Asian aerosols on the East Asian summer monsoon: roles of aerosol–radiation and aerosol–cloud interactions. *Clim Dyn* 53, 3235–3256. https://doi.org/10.1007/s00382-019-04698-0.

Dong, Y., Kay, J. E., Deser, C., Capotondi, A., and Sanchez, S. C., 2024: Distilling the evolving contributions of anthropogenic aerosols and greenhouse gases to large-scale low-frequency surface ocean changes over the past century. *Geophysical Research Letters*, 51, e2024GL112020. https://doi.org/10.1029/2024GL112020.

England, M.R., Eisenman, I., Lutsko, N.J., and Wagner, T.J., 2021: The recent emergence of Arctic amplification. *Geophysical Research Letters*, 48(15), p.e2021GL094086, https://doi.org/10.1029/2021GL094086.

Fasullo, J.T., Lamarque, J.F., Hannay, C., Rosenbloom, N., Tilmes, S., DeRepentigny, P., Jahn, A., and Deser, C., 2022: Spurious late historical-era warming in CESM2 driven by prescribed biomass burning emissions. *Geophysical Research Letters*, 49(2), p.e2021GL097420, https://doi.org/10.1029/2021GL097420.

840 Flynn, C. M. and Mauritsen, T., 2020: On the climate sensitivity and historical warming
841 evolution in recent coupled model ensembles, Atmos. Chem. Phys., 20, 7829–7842,
842 https://doi.org/10.5194/acp-20-7829-2020.

843 Gillett, Z. E., H. H. Hendon, J. M. Arblaster, H. Lin, and D. Fuchs, 2022: On the Dynamics
844 of Indian Ocean Teleconnections into the Southern Hemisphere during Austral Winter. *J.*
845 *Atmos. Sci.*, 79, 2453–2469, https://doi.org/10.1175/JAS-D-21-0206.1.

846 Gregory, J.M., Ingram, W.J., Palmer, M.A., Jones, G.S., Stott, P.A., Thorpe, R.B., Lowe,
847 J.A., Johns, T.C. and Williams, K.D., 2004: A new method for diagnosing radiative
848 forcing and climate sensitivity. *Geophysical research letters*, *31*(3),
849 doi:10.1029/2003GL018747.

850 Heyblom, K.B., Singh, H.A., Rasch, P.J., and Hirasawa, H., 2023: Variability in biomass
851 burning emissions weakens aerosol forcing due to nonlinear aerosol-cloud
852 interactions. *Geophysical Research Letters*, *50*(11), p.e2022GL102685,
853 https://doi.org/10.1029/2022GL102685.

854 He, J., and B. J. Soden, 2015: Anthropogenic Weakening of the Tropical Circulation: The
855 Relative Roles of Direct CO2 Forcing and Sea Surface Temperature Change. *J.*
856 *Climate*, 28, 8728-8742, https://doi.org/10.1175/JCLI-D-15-0205.1.

857 Hill, S. A., Y. Ming, and I. M. Held, 2015: Mechanisms of Forced Tropical Meridional
858 Energy Flux Change. *J. Climate*, 28, 1725–1742, https://doi.org/10.1175/JCLI-D-14-
859 00165.1.

860 Hirasawa, H., P. J. Kushner, M. Sigmond, J. Fyfe, and C. Deser, 2020: Anthropogenic
861 Aerosols Dominate Forced Multidecadal Sahel Precipitation Change through Distinct
862 Atmospheric and Oceanic Drivers. *J. Climate*, 33, 10187-
863 10204, https://doi.org/10.1175/JCLI-D-19-0829.1.

864 Holland, M.M., Hannay, C., Fasullo, J., Jahn, A., Kay, J.E., Mills, M., Simpson, I.R., Wieder,
865 W., Lawrence, P., Kluzek, E., and Bailey, D., 2024: New model ensemble reveals how
866 forcing uncertainty and model structure alter climate simulated across CMIP generations
867 of the Community Earth System Model. *Geoscientific Model Development*, *17*(4),
868 pp.1585-1602, https://doi.org/10.5194/gmd-17-1585-2024.

869 Hoskins, B. J., and T. Ambrizzi, 1993: Rossby Wave Propagation on a Realistic
870 Longitudinally Varying Flow. *J. Atmos. Sci.*, 50, 1661-
871 1671, https://doi.org/10.1175/1520-0469(1993)050<1661:RWPOAR>2.0.CO;2.

872 Hua, W., Dai, A., Zhou, L., Qin, M. and Chen, H., 2019: An externally forced decadal
873 rainfall seesaw pattern over the Sahel and southeast Amazon. *Geophysical Research*
874 *Letters*, 46, 923–932, https://doi.org/10.1029/2018GL081406.

875 Hua, W., Lou, S., Huang, X., Xue, L., Ding, K., Wang, Z., and Ding, A., 2024: Diagnosing
876 uncertainties in global biomass burning emission inventories and their impact on modeled
877 air pollutants, Atmos. Chem. Phys., 24, 6787–6807, https://doi.org/10.5194/acp-24-6787-
878 2024.

879 Hwang, Y.-T., D. M. W. Frierson, and S. M. Kang, 2013: Anthropogenic sulfate aerosol and
880 the southward shift of tropical precipitation in the late 20th century. *Geophys. Res.*
881 *Lett.*, 40, 2845–2850, doi:10.1002/grl.50502.

882 Hwang, Y.T., Xie, S.P., Chen, P.J., Tseng, H.Y., and Deser, C., 2024: Contribution of
883 anthropogenic aerosols to persistent La Niña-like conditions in the early 21st
884 century. *Proceedings of the National Academy of Sciences*, *121*(5), p.e2315124121,
885 https://doi.org/10.1073/pnas.2315124121.

886 IPCC AR6: Szopa, S., Naik, V., Adhikary, B., Artaxo, P., Berntsen, T., Collins, W.D., Fuzzi,
887 S., Gallardo, L., Kiendler-Scharr, A., Klimont, Z. and Liao, H., 2021: Short-Lived
888 Climate Forcers (Chapter 6).

889 Kang, J.M., Shaw, T.A. and Sun, L., 2024: Anthropogenic aerosols have significantly
890 weakened the regional summertime circulation in the Northern Hemisphere during the
891 satellite era. *AGU Advances*, 5, 2024AV001318, https://doi.org/10.1029/2024AV001318.

892 Kang, S.M., Xie, S.P., Deser, C., and Xiang, B., 2021: Zonal mean and shift modes of
893 historical climate response to evolving aerosol distribution. *Science Bulletin*, *66*(23),
894 pp.2405-2411, https://doi.org/10.1016/j.scib.2021.07.013.

895 Kay, J. E., and Coauthors, 2015: The Community Earth System Model (CESM) Large
896 Ensemble Project: A Community Resource for Studying Climate Change in the Presence
897 of Internal Climate Variability. *Bull. Amer. Meteor. Soc.*, 96, 1333–
898 1349, https://doi.org/10.1175/BAMS-D-13-00255.1.

899 Lawrence, D.M., and Coauthors, 2011: Parameterization improvements and functional and
900 structural advances in version 4 of the Community Land Model. *Journal of Advances in*
901 *Modeling Earth Systems*, *3*(1), doi:10.1029/2011MS00045.

902 Lamarque, J.-F., Bond, T. C., Eyring, V., Granier, C., Heil, A., Klimont, Z., Lee, D., Liousse,
903 C., Mieville, A., Owen, B., Schultz, M. G., Shindell, D., Smith, S. J., Stehfest, E., Van
904 Aardenne, J., Cooper, O. R., Kainuma, M., Mahowald, N., McConnell, J. R., Naik, V.,
905 Riahi, K., and van Vuuren, D. P.: Historical (1850–2000) gridded anthropogenic and
906 biomass burning emissions of reactive gases and aerosols: methodology and application,
907 Atmos. Chem. Phys., 10, 7017–7039, https://doi.org/10.5194/acp-10-7017-2010.

908 Li, S., Liu, W., Allen, R.J., Shi, J.R. and Li, L., 2023: Ocean heat uptake and interbasin
909 redistribution driven by anthropogenic aerosols and greenhouse gases. *Nat.*
910 *Geosci.*, *16*(8), pp.695-703, https://doi.org/10.1038/s41561-023-01219-x.

911 Li, X., Ting, M., You, Y., Lee, D.-E., Westervelt, D. M., & Ming, Y., 2020: South Asian
912 summer monsoon response to aerosol-forced sea surface temperatures. Geophysical
913 Research Letters, 47, e2019GL085329. https://doi.org/10.1029/2019GL085329.

914 Li, Y., J. Li, F. F. Jin, and S. Zhao, 2015: Interhemispheric Propagation of Stationary Rossby
915 Waves in a Horizontally Nonuniform Background Flow. *J. Atmos. Sci.*, 72, 3233–
916 3256, https://doi.org/10.1175/JAS-D-14-0239.1.

917 Li, X., Cai, W., Meehl, G.A. et al., 2021: Tropical teleconnection impacts on Antarctic
918 climate changes. Nat Rev Earth Environ 2, 680–698, https://doi.org/10.1038/s43017-021-
919 00204-5.

920 Li, X., Ting, M. and Lee, D.E., 2018. Fast adjustments of the Asian summer monsoon to
921 anthropogenic aerosols. Geophysical Research Letters, 45(2), pp.1001-1010.
922 https://doi.org/10.1002/2017GL076667.

923 Liu, X., Easter, R.C., Ghan, S.J., Zaveri, R., Rasch, P., Shi, X., Lamarque, J.F., Gettelman,
924 A., Morrison, H., Vitt, F., and Conley, A., 2012: Toward a minimal representation of
925 aerosols in climate models: Description and evaluation in the Community Atmosphere
926 Model CAM5. *Geoscientific Model Development*, *5*(3), pp.709-739,
927 https://doi.org/10.5194/gmd-5-709-2012.

928 Liu, F., Li, X., Luo, Y., Cai, W., Lu, J., Zheng, X.T., Kang, S.M., Wang, H., and Zhou, L.,
929 2024: Increased Asian aerosols drive a slowdown of Atlantic meridional overturning

circulation. Nature Communications, 15(1), p.18, https://doi.org/10.1038/s41467-023-44597-x.

Liu, L., and Coauthors, 2018: A PDRMIP Multimodel Study on the Impacts of Regional Aerosol Forcings on Global and Regional Precipitation. *J. Climate*, 31, 4429–4447, https://doi.org/10.1175/JCLI-D-17-0439.1.

Lund, M. T., Myhre, G., and Samset, B. H., 2019: Anthropogenic aerosol forcing under the Shared Socioeconomic Pathways, Atmos. Chem. Phys., 19, 13827–13839, https://doi.org/10.5194/acp-19-13827-2019.

Menary, M.B., and Coauthors, 2020: Aerosol-forced AMOC changes in CMIP6 historical simulations. *Geophysical Research Letters*, *47*(14), p.e2020GL088166, https://doi.org/10.1029/2020GL088166.

Ming, Y., and V. Ramaswamy, 2011: A Model Investigation of Aerosol-Induced Changes in Tropical Circulation. *J. Climate*, 24, 5125-5133, https://doi.org/10.1175/2011JCLI4108.1.

Morrison, H., and A. Gettelman, 2008: A New Two-Moment Bulk Stratiform Cloud Microphysics Scheme in the Community Atmosphere Model, Version 3 (CAM3). Part I: Description and Numerical Tests. *J. Climate*, 21, 3642-3659, https://doi.org/10.1175/2008JCLI2105.1.

Mueller, B. L., N. P. Gillett, A. H. Monahan, and F. W. Zwiers, 2018: Attribution of Arctic Sea Ice Decline from 1953 to 2012 to Influences from Natural, Greenhouse Gas, and Anthropogenic Aerosol Forcing. *J. Climate*, 31, 7771-7787, https://doi.org/10.1175/JCLI-D-17-0552.1.

Nabat, P., Somot, S., Boé, J., Corre, L., Katragkou, E., Li, S., Mallet, M., van Meijgaard, E., Pavlidis, V., Pietikäinen, J.P., and Sørland, S., 2025: Multi-model assessment of the role of anthropogenic aerosols in summertime climate change in Europe. *Geophysical Research Letters*, 52, e2024GL112474, https://doi.org/10.1029/2024GL112474.

Neale, R.B., Chen, C.C., Gettelman, A., Lauritzen, P.H., Park, S., Williamson, D.L., Conley, A.J., Garcia, R., Kinnison, D., Lamarque, J.F., and Marsh, D., 2010: Description of the NCAR community atmosphere model (CAM 5.0). *NCAR Tech. Note NCAR/tn-486+STR*, *1*(1), pp.1-12.

959 North, G. R., T. L. Bell, R. F. Cahalan, and F. J. Moeng, 1982: Sampling errors in the
960 estimation of empirical orthogonal functions. *Mon. Wea. Rev.*, **110 ,** 699–706.

961 Persad, G.G., and Caldeira, K., 2018: Divergent global-scale temperature effects from
962 identical aerosols emitted in different regions. *Nature Communications*, *9*(1), p.3289,
963 https://doi.org/10.1038/s41467-018-05838-6.

964 Persad, G. G., D. J. Paynter, Y. Ming, and V. Ramaswamy, 2017: Competing Atmospheric
965 and Surface-Driven Impacts of Absorbing Aerosols on the East Asian Summertime
966 Climate. J. Climate, 30, 8929–8949, https://doi.org/10.1175/JCLI-D-16-0860.1.

967 Persad, G.G., Cummins, C. and Baldwin, J.W., 2025: Anthropogenic aerosol changes
968 disproportionately impact the evolution of global heatwave hazard and
969 exposure. *Environmental Research Letters*, *20*(8), p.084023.

970 Persad, G., Samset, B.H., Wilcox, L.J., Allen, R.J., Bollasina, M.A., Booth, B.B., Bonfils, C.,
971 Crocker, T., Joshi, M., Lund, M.T. and Marvel, K., 2023: Rapidly evolving aerosol
972 emissions are a dangerous omission from near-term climate risk assessments.
973 Environmental Research: Climate, 2(3), p.032001.

974 Rodgers, K. B., S. -S. Lee, N. Rosenbloom, A. Timmermann, G. Danabasoglu, C. Deser, J.
975 Edwards, J. -E. Kim, I. Simpson, K. Stein, M. F. Stuecker, R. Yamaguchi, T. Bodai, E. -
976 S. Chung, L. Huang, W. Kim, J. -F. Lamarque, D. Lombardozzi, W. R. Wieder and S. G.
977 Yeager, 2021: Ubiquity of human-induced changes in climate variability. *Earth Sys.*
978 *Dyn.*, **12**, 1393–1411, doi:10.5194/esd-12-1393-2021.

979 Roesch, C.M., Fons, E., Ballinger, A.P. *et al.,* 2025: Decreasing aerosols increase the
980 European summer diurnal temperature range. *npj Clim Atmos Sci* 8, 47.
981 https://doi.org/10.1038/s41612-025-00922-3

982 Samset, B.H., Myhre, G., Forster, P.M., Hodnebrog, Ø., Andrews, T., Faluvegi, G.,
983 Flaeschner, D., Kasoar, M., Kharin, V., Kirkevåg, A., and Lamarque, J.F., 2016: Fast and
984 slow precipitation responses to individual climate forcers: A PDRMIP multimodel
985 study. *Geophysical research letters*, *43*(6), pp.2782-2791, doi:10.1002/2016GL068064.

986 Scholten, R.C., Veraverbeke, S., Chen, Y., and Randerson, J.T., 2024: Spatial variability in
987 Arctic–boreal fire regimes influenced by environmental and human factors. *Nature*
988 *Geoscience*, *17*(9), pp.866-873, https://doi.org/10.1038/s41561-024-01505-2.

989 Schumacher, D.L., Singh, J., Hauser, M., Fischer, E.M., Wild, M. and Seneviratne, S.I.,
990 2024: Exacerbated summer European warming not captured by climate models neglecting
991 long-term aerosol changes. *Communications Earth & Environment*, *5*(1), p.182,
992 https://doi.org/10.1038/s43247-024-01332-8.

993 Shaw, T., Voigt, A., 2015: Tug of war on summertime circulation between radiative forcing
994 and sea surface warming. Nature Geosci 8, 560–566, https://doi.org/10.1038/ngeo2449.

995 Shawki, D., Voulgarakis, A., Chakraborty, A., Kasoar, M., & Srinivasan, J., 2018: The South
996 Asian monsoon response to remote aerosols: Global and regional mechanisms. Journal of
997 Geophysical Research: Atmospheres, 123, 11,585–11,601,
998 https://doi.org/10.1029/2018JD028623.

999 Shi, J., Kwon, Y., and Wijffels, S. E., 2022: Two Distinct Modes of Climate Responses to the
1000 Anthropogenic Aerosol Forcing Changes. *J. Climate*, 35, 3445–
1001 3457, https://doi.org/10.1175/JCLI-D-21-0656.1.

1002 Shindell, D., Faluvegi, G., 2009: Climate response to regional radiative forcing during the
1003 twentieth century. Nature Geosci 2, 294–300. https://doi.org/10.1038/ngeo473.

1004 Smith, D.M., and Coauthors, 2016: Role of volcanic and anthropogenic aerosols in the recent
1005 global surface warming slowdown. *Nature Climate Change*, *6*(10), pp.936-940,
1006 https://doi.org/10.1038/nclimate3058.

1007 Sutton, R., Dong, B. 2012: Atlantic Ocean influence on a shift in European climate in the
1008 1990s. *Nature Geosci* 5, 788–792. https://doi.org/10.1038/ngeo1595.

1009 Takemura, T., 2012: Distributions and climate effects of atmospheric aerosols from the
1010 preindustrial era to 2100 along Representative Concentration Pathways (RCPs) simulated
1011 using the global aerosol model SPRINTARS, Atmos. Chem. Phys., 12, 11555–11572,
1012 https://doi.org/10.5194/acp-12-11555-2012.

1013 Tian, Y., Hu, S., and Deser, C., 2023: Critical role of biomass burning aerosols in enhanced
1014 historical Indian Ocean warming. *Nature Communications*, *14*(1), p.3508,
1015 https://doi.org/10.1038/s41467-023-39204-y.

1016 Undorf, S., M. A. Bollasina, and G. C. Hegerl, 2018a: Impacts of the 1900–74 Increase in
1017 Anthropogenic Aerosol Emissions from North America and Europe on Eurasian Summer
1018 Climate. *J. Climate*, 31, 8381–8399, https://doi.org/10.1175/JCLI-D-17-0850.1.

1019 Undorf, S., Polson, D., Bollasina, M. A., Ming, Y., Schurer, A., & Hegerl, G. C., 2018b:
1020 Detectable impact of local and remote anthropogenic aerosols on the 20th century
1021 changes of West African and South Asian monsoon precipitation. Journal of Geophysical
1022 Research: Atmospheres, 123, 4871–4889. https://doi.org/10.1029/2017JD027711.

1023 Van Der Werf, G.R., Randerson, J.T., Giglio, L., Van Leeuwen, T.T., Chen, Y., Rogers,
1024 B.M., Mu, M., Van Marle, M.J., Morton, D.C., Collatz, G.J., and Yokelson, R.J., 2017:
1025 Global fire emissions estimates during 1997–2016. *Earth System Science Data*, *9*(2),
1026 pp.697-720, https://doi.org/10.5194/essd-9-697-2017.

1027 Wang, H., and Wen, Y.J., 2022: Climate response to the spatial and temporal evolutions of
1028 anthropogenic aerosol forcing. *Climate Dynamics*, *59*(5), pp.1579-1595,
1029 https://doi.org/10.1007/s00382-021-06059-2.

1030 Wang, H., S. Xie, Y. Kosaka, Q. Liu, and Y. Du, 2019: Dynamics of Asian Summer
1031 Monsoon Response to Anthropogenic Aerosol Forcing. J. Climate, 32, 843–858,
1032 https://doi.org/10.1175/JCLI-D-18-0386.1.

1033 Wang, H., Zheng, X., Cai, W., Han, Z., Xie, S., Kang, S.M., Geng, Y., Liu, F., Wang, C.,
1034 Wu, Y. Xiang, B. & Zhou, L., 2024: Atmosphere teleconnections from abatement of
1035 China aerosol emissions exacerbate Northeast Pacific warm blob events, Proc. Natl.
1036 Acad. Sci. U.S.A. 121 (21) e2313797121, https://doi.org/10.1073/pnas.2313797121.

1037 Wang, Z., Lin, L., Xu, Y., Che, H., Zhang, X., Zhang, H., Dong, W., Wang, C., Gui, K.. and
1038 Xie, B., 2021: Incorrect Asian aerosols affecting the attribution and projection of regional
1039 climate change in CMIP6 models. *npj Climate and Atmospheric Science*, *4*(1), p.2,
1040 https://doi.org/10.1038/s41612-020-00159-2.

1041 Westervelt, D. M., You, Y., Li, X., Ting, M., Lee, D. E., & Ming, Y., 2020: Relative
1042 importance of greenhouse gases, sulfate, organic carbon, and black carbon aerosol for
1043 South Asian monsoon rainfall changes. Geophysical Research Letters, 47,
1044 e2020GL088363, https://doi.org/10.1029/2020GL088363.

1045 White, K., G. Persad, Samset, B.H. and coauthors, 2025: Anthropogenic Aerosols Dominate
1046 the Forced Contribution to Historical Precipitation Trends in Populated Regions,
1047 *Proceedings of the National Academy of Sciences* (under review).

1048 Wilcox, L.J., Allen, R.J., Samset, B.H., Bollasina, M.A., Griffiths, P.T., Keeble, J., Lund,
1049 M.T., Makkonen, R., Merikanto, J., O'Donnell, D., and Paynter, D.J., 2023: The regional

aerosol model intercomparison project (RAMIP). *Geoscientific Model Development*, *16*(15), pp.4451-4479, https://doi.org/10.5194/gmd-16-4451-2023.

Wilks, D. S., 2016: "The Stippling Shows Statistically Significant Grid Points": How Research Results are Routinely Overstated and Overinterpreted, and What to Do about It. Bull. Amer. Meteor. Soc., 97, 2263–2273, https://doi.org/10.1175/BAMS-D-15-00267.1.

Xiang, B., Xie, S.P., Kang, S.M., and Kramer, R.J., 2023: An emerging Asian aerosol dipole pattern reshapes the Asian summer monsoon and exacerbates northern hemisphere warming. *npj Climate and Atmospheric Science*, *6*(1), p.77, https://doi.org/10.1038/s41612-023-00400-8.

Xie, S.P., Lu, B. and Xiang, B., 2013: Similar spatial patterns of climate responses to aerosol and greenhouse gas changes. *Nature Geosci*, *6*(10), pp.828-832, https://doi.org/10.1038/ngeo1931.

Zelinka, M. D., T. Andrews, P. M. Forster, and K. E. Taylor, 2014: Quantifying components of aerosol–cloud–radiation interactions in climate models. J. Geophys. Res. Atmos., 119, 75997615, https://doi.org/10.1002/2014jd021710.

Zhang, Y., Shindell, D., Seltzer, K., Shen, L., Lamarque, J.-F., Zhang, Q., Zheng, B., Xing, J., Jiang, Z., and Zhang, L., 2021: Impacts of emission changes in China from 2010 to 2017 on domestic and intercontinental air quality and health effect, Atmos. Chem. Phys., 21, 16051–16065, https://doi.org/10.5194/acp-21-16051-2021.